



## CDF ENDCAP E.M. CALORIMETER AND TEST RESULTS

S. Mikamo and M. Mishina\*

National Laboratory for High Energy Physics, KEK, Ibaraki-ken, Japan

and

Y. Hayashide, T. Kamon, S. Kim, K. Kondo, S. Miyashita, H. Miyata, F. Sato,  
Y. Takaiwa, A. Yamashita, and Y. Yasu  
University of Tsukuba, Ibaraki-ken, Japan

and

Y. Muraki  
Institute for Cosmic Ray Research, University of Tokyo, Tanashi-shi,  
Tokyo, Japan

and

A. Murakami  
Saga University, Saga-shi, Japan

and

M. Atac, J. E. Freeman, D. R. Hanssen, J. C. Urish, R. Yamada, and J. Yoh  
Fermi National Accelerator Laboratory, Batavia, Illinois 60510, USA

March 1983

\*Presenter at the Gas Sampling Calorimetry Workshop, October 28-29, 1982,  
Fermi National Accelerator Laboratory, Batavia, Illinois 60510 USA

S.Mikamo, M.Mishina  
 National Laboratory for High Energy Physics, KEK, Ibaraki-ken, Japan  
 Y.Hayashide, T.Kamon, S.Kim, K.Kondo, S.Miyashita, H.Miyata, F.Sato,  
 Y.Takaiwa, A.Yamashita, Y.Yasu  
 University of Tsukuba, Ibaraki-ken, Japan  
 Y.Muraki  
 Institute for Cosmic Ray Research, University of Tokyo, Tanashi-shi, Tokyo, Japan  
 A.Murakami  
 Saga University, Saga-shi, Japan  
 M.Atac, J.E.Freeman, D.R.Hanssen, J.C.Urish, R.Yamada, J.Yoh  
 Fermi National Accelerator Laboratory, Batavia, IL 60510, U.S.A.

## ABSTRACT

We have developed an electromagnetic calorimeter composed of proportional tubes and lead layers. The proportional tubes were made out of conductive plastic tubes and 50  $\mu$ m wires which made a complete conical geometry possible with reading out appropriately patterned pick up electrodes on the outside of the tubes. Two generations of prototype modules have been built and tested by high energy electrons and hadrons. Good energy resolution and position resolution were obtained. Other properties were also extensively studied.

## CONDITIONS AND REQUIREMENTS

The Collider Detector at Fermilab<sup>1)</sup> is currently under construction for use at 2000 GeV  $\bar{p}p$  colliding beam experiment in the near future. It is essentially a cylindrical system in which a large and strong superconducting solenoid is surrounded by calorimeters almost in entire solid angle together with partial coverage of muon detectors. The solenoid is 3 meter in diameter, 5 meter long, and 15 kGauss. Calorimeters are all composed of electromagnetic calorimeter layers in front and hadron calorimeter layers behind.

The role of the calorimeters is to measure the energy flow as a function of the polar and the azimuthal angles, and to identify more or less isolated electrons. For these purposes the calorimeters have to be segmented both laterally and longitudinally, and the segmentation must be done in a conical geometry around the interaction region.

The end cap electromagnetic calorimeter is designed to cover the both ends of the solenoid. The cross sectional view is shown in Fig. 1. It subtends an acceptance of  $10^\circ$  to  $36^\circ$  with respect to the beam axis both in the forward and the backward directions. Since it is positioned deep in the 15 kGauss solenoidal field, and also, there is a thick return yoke structure right behind it, which is also layered with steel plates and proportional tube layers to form hadron calorimeter, scintillator based scheme was abandoned from the beginning because of its difficulties due to the sensitiveness of phototubes to the magnetic field. It is also conceived to be difficult to segment scintillators laterally and longitudinally fine enough without introducing significant dead space. Then one of the viable choices is a proportional chamber calorimeter.

We can avail of a fair number of data on chamber calorimeters by various authors<sup>2)</sup> today which includes those designed for large colliding beam detectors. All of the existing test data fit the following formula in their energy resolution

$$\sigma_E / E = k \sqrt{t / E} \%$$

with  $k$  of 30 to 35<sup>3)</sup>, where  $t$  is the sampling thickness in radiation length and  $E$  in GeV. At present we have our own data which also fall in this category. The above expression reduces to

$$\sigma_E / E = k' / \sqrt{E} \%$$

with  $k'$  of 24 to 25 if we take 0.5 as a typical value of  $t$ .

What do we expect in our case of the Collider Detector at Fermilab? One of the measures of interesting physics is the transverse momentum  $P_T$  of the observed particles. As a typical example of the predicted phenomena to be observed in this particular angular region is the asymmetry of the positive and the negative charge leptons from leptonic decays of weak bosons  $W_{\pm}$ . In Fig. 2 the differential cross sections of positive and negative lepton production via  $W$  decay are plotted against  $P_T$ <sup>4)</sup>. There is a distinctive difference in the  $P_T$  dependence especially in smaller polar angles between the positive and the negative leptons. The excess of the negative leptons over the positive leptons in lower  $P_T$  region in this proton forward hemisphere is the manifestation of weak V-A structure. In this figure we can also visualize that  $P_T$  is a good parameter to measure the physics common to different angles. Then this  $P_T$  dependence is translated by a factor  $1/\sin\theta$  into laboratory momentum dependence shown in Fig. 3. In the angular range the end cap calorimeter subtends, the linear laboratory momentum extends to 225 GeV because of the factor of 1.7 to 5.6.

Then the energy resolution goes down to 1.4 to 1.7 according to the previous discussion which is close to the limit of systematic errors. Therefore the choice of the proportional chamber as the sampling media for the electromagnetic calorimeter in this angular region is reasonable with regard to the energy resolution.

For a proportional chamber system it is crucial to maintain uniformity of the mechanical dimensions, especially the gap height between the cathode planes to have uniform response. As usually done, we have decided to use repeated cell structure with stringing an anode wire in each of the cells. Usually extrusion of such structure gives excellent dimensional tolerance leaving little worry in making the cell dimensions uniform.

It should be noted that in this angular region the effect of the finite length of the interaction region along the beam is not significant as seen in Fig. 1. Therefore it is desirable to segment the calorimeter into conical tower geometry with each tower subtending a definite solid angle with respect to the center of the interaction region. Such conical tower geometry can be materialized easily by using cathode pick-up electrodes with an appropriate segmentation without introducing any dead space, instead of anode wire read-out. It is possible to use aluminum extrusion with regularly repeated partitions with a cover with appropriately patterned pick-up electrodes on the inside. Also it is possible to use resistive sheet as the cover for such structure which allows one to isolate the electrostatic high voltage field from the pick-up electrode. However, such a structure needs a skilled labor to insulate electrically the inner surface of the cover from the aluminum ribs still holding the cover tight enough. Other possibility is to coat plastic cell structure with conductive paint which also needs a delicate control of the process.

After such considerations, we have chosen conductive plastic tube array. In this the mechanical precision and the resistivity uniformity is controlled at one point in the production process, i.e. at the time of the extrusion. Then the pick-up electrodes can be easily made by etching necessary pattern on copper clad

G-10 board and glueing it onto the tube array. With this structure both sides can be used for read-out in contrast to aluminum extrusion. Also even for an application in which single side read-out is enough, the signal is half of the anode wire signal for the conductive plastic tubes, and about a quarter for the aluminum extrusion. Such a panel with G-10 boards on both sides of the tube array is quite stiff and there is no problem of thermal distortion of the chamber because of very low thermal expansion coefficient of the G-10 board on both sides.

The space allocated to the end cap electromagnetic calorimeter is 21 inches along the beam axis and the space to lead the signal cables to the electronic modules on the outside is also quite restricted. Proportional chamber system does not suffer from such constraint too much.

## STRUCTURE OF THE CDF END CAP ELECTROMAGNETIC CALORIMETER

Once conductive plastic tube is chosen as the proportional tube element, the layout of the outside pick-up electrodes is unrestricted in its pattern. Fig. 4 shows the layout of the pads to be etched on one side of the copper clad G-10 boards on every chamber layer. Basic  $\Delta\phi = 30^\circ$  panels are further segmented radially based on pseudo rapidity variable, and azimuthally into  $\Delta\phi = 5^\circ$ . The inner radius is defined by a conical vessel wall of  $\theta = 10^\circ$ , and the outer radius is defined by a cylindrical vessel wall with outer dimension of  $r=55"$ . Fig. 1 illustrates the cross sectional view of such radial segmentation with broken lines showing the flaring of the tower with the depth. It is seen that the broadening of the polar angle definition of the hit points on the surface due to the finite length of the interaction region is not significant.

The basic  $30^\circ$ -sector of each sampling layer is sketched in Fig. 5. An array of conductive plastic tubes are stacked with two G-10 boards. The copper plating etched into pads, on the bottom G-10 panel, is facing the tube array. Every chamber has such a pad panel on one side and a plain copper plating on the opposite side as a ground plane except for those layers around shower maximum which have either  $\theta$ - or  $\phi$ -strips on the opposite sides. Therefore the lines on the top G-10 panel in this figure is merely to show how the signal from individual pad is lead to the edge card connectors on the outer radius by strip lines on the rear side of the pad-etched panel shown at the bottom. The cross sectional dimensions of the conductive plastic tubes are indicated in Fig. 6. The tubes for the first prototype had a wall thickness of 1.5 mm but we have been successful in reducing it to half as shown in the figure for the second prototype. With a 50  $\mu$ m gold plated tungsten wire,  $Fe^{55}$  pulse height spectrum is obtained as shown in Fig. 7.

We have made two generations of prototype modules using the technique described above and tested them by high energy electron and hadron beams at Fermilab.

## FIRST PROTOTYPE MODULE<sup>5)</sup>

The first prototype module of the CDF end cap electromagnetic was built in 1981 spring using conductive plastic proportional tubes. In Table 1 the parameters are compared with those for the second prototype module built in 1982 spring using the conductive plastic tubes with exactly the same cell dimensions except the wall thickness. Essentially the first prototype was to prove that such conductive plastic tubes were stable for proportional tube operation and also to prove that external electrode pick-up is usable to materialize fine lateral segmentation still measuring the total energy with decent accuracy.

As tabulated in Table 2, the stack was divided into three longitudinal segments and the pads at the same solid angle element are connected together in depth within the same longitudinal segment. The lead panels were 2 mm thick in the second segment and were thicker in the rest of the segments. There were five chambers with  $\theta$ -strips on one side and  $\phi$ -strips on the other side which were individually read out. The anode wires in  $\theta$ - and  $\phi$ -strip chambers were read out individually. The anode wires in the pad-chambers were connected together in the same chamber and read out chamber by chamber. Total thickness of the module was 20.3 radiation length. Figs. 8 a, b, and c show the patterns of the outside pick-up electrodes, pads,  $\theta$ -strips, and  $\phi$ -strips. Fig. 9 is a sketch of a layer of  $90^\circ$  sector.

The module was tested at Fermilab M-5 beam line. The beam was a negative charged mixed beam of variable energies from 10 to 46 GeV within which electrons were identified by two He-filled threshold Cerenkov counters. The beam was defined by a trigger counter vetoed by an about 1-ft<sup>2</sup> large veto counter with a square hole of about 1 in<sup>2</sup>.

The gas was 50 %-50 % Ar-ethane with 1.4 % admixture of ethylalcohol.

The longitudinal development of the electron- and hadron-induced showers were observed as shown in Fig. 10. There is a distinctive difference between electrons and hadrons which can be used for electron identification.

The total charge collected on the wire and on the pick-up electrodes are plotted in Fig. 11. It is seen that the sum of the cathode signal is essentially equal to the anode wire signal. The response is quite linear within this energy range up to 46 GeV. The energy resolution for the anode wire signal and cathode signal are plotted against  $1/\sqrt{E}$  in Fig. 12. It is seen that the energy resolutions for the anode signals and the cathode signals are exactly the same. The measured points are well fitted by  $1/\sqrt{E}$  as expected. Since every layer was read out, we can reproduce the case of coarser sampling thickness with adding up every other layer, every third layer, and so on by the software manipulation. The results are plotted in Fig. 13. For every case,  $1/\sqrt{E}$  dependence is seen and these dependence was consistent with a single expression

$$\sigma_E/E = 30 \sqrt{t/E} \%$$

with  $t$ , the sampling thickness of each layer in radiation length, and  $E$  in GeV, except for the 2-mm sampling which is about  $36 \sqrt{t/E} \%$ .

Utilizing the lateral distribution of the shower over pads and strips, together with wires those which read out individually, we can find the incident point as the centroid of the lateral pulse height distributions. The accuracy of such measurement is evaluated by plotting event-by-event deviation of the calculated centroid from the real incident point measured by the beam pwc's in front of the calorimeter. Fig. 14 shows the distribution for 40 GeV electron beam. The r.m.s. error of such distribution is plotted in Fig. 15 against the incident electron energies. It is understandable that the second longitudinal segment of the pads is most accurate because it contains most of the shower energy while second  $\theta$ - $\phi$  chambers sample the shower profile at one point in the depth being subject to layer to layer fluctuation.

## SECOND PROTOTYPE MODULE <sup>6)</sup>

The second prototype module was built and tested in spring of 1982.

As listed in Table 1, this module is almost exactly the same as the first

prototype module in its basic chamber structure except that the wall thickness of the conductive plastic tubes was reduced to 0.8 mm. Otherwise the tube cell dimensions and the way of stacking the tube arrays with G-10 boards is the same as the previous one.

Major difference of the second prototype is that this  $\Delta\varphi = 30^\circ$  sector module is quite close to the final design in its size, and the segmentation. The radius was about 1.4 meter and the pads were segmented in almost the same step as the final design in the radius and segmented into 5 each in c. Also the layout of the strip lines from individual pads and  $\theta$ - $\varphi$  strips to edge card connectors and the cabling of the signals were done in a realistic manner.

The lead panels were 3 mm thick samely as the final design. The sketch of the module is shown in Fig. 16. In order to test the response of such conical towers, a mount was designed which was rotatable both horizontally around a postulated center of the interaction region on the beam line to reproduce the polar angle, and vertically around the beam axis to reproduce the azimuthal angle of any selected tower.

The configuration of the second prototype module is listed in Table 3. All thirty eight chamber had pads on one side and the opposite sides were either plain grounded copper plating for those in the first and the third segments, or,  $\theta$ - or  $\varphi$ -strips for those in the second longitudinal segment.  $\theta$ - and  $\varphi$ -strips were interleaved with each other and longitudinally segmented into two sections individually. The layout of the pads,  $\theta$ -strips, and  $\varphi$ -strips are shown in Figs. 17 a, b, and c, respectively. Notice that  $\theta$ - and  $\varphi$ -strips are about five times finer in one direction than the pads at the same place in most of the surface while in the other dimension they give pulse height distribution integrated over the sector. This is because the role of the strips are to examine in detail the structure of the large energy deposit found by the pad towers to test whether the detected large shower has single core or not.

Fig. 18 a shows the anode wire connections schematically. All the anode wires in the same plane are bussed together through individual 100 ohm resistors and connected to high voltage bus line through a 100 kohm protection resistor. The signal from the wires is branched before the 100 kohm resistor for signal read out. The signal is then lead to LRS 2285A 15 bit ADC modules layer by layer via 55 meter long, 280 nsec delay, RG 58/U equivalent 50 ohm coaxial cables.

The pads at the same solid angle element are connected together in the depth into three longitudinal segments. The connection was done directly attaching edge card connectors onto flat cables. The signals were then transmitted to the ADC's in an identical way as the anode wire signals. Fig. 18b schematically shows such connection. In order to invert the positive signals from the pads, a small core transformer was used at the end of each of the cables.

The gas was again 50 % - 50 % Ar-ethane with 1.4 % admixture of ethylalcohol.

The test was done at Fermilab M-4 beam line. The arrangement is schematically shown in Fig. 19. Using the secondary particles from a production target, The beam line provided either of pure electrons or mixed charged particles. The electron beam was produced by converting neutral particle,  $\gamma$ 's from  $\pi^0$ 's, by a lead plate after all the charged particles were swept away by a sweeping magnet. The purity, judging from the on-line histograms of the calorimeter pulse height distributions shown in Figs. 21 a through d, was better than  $10^3$ . Conversely, when the hadron beam was required, all the neutral particles were shaken off by bending magnet triplet while the sweeper was turned off. Although the total momentum bite of the beam was broad, electron momenta were precisely measured event-by-event using two sets of analyzing magnets with five sets of

pwc's of 1 mm wire spacings. The r.m.s. momentum resolution was nominally 0.14 % with slight degradation due to the multiple scattering from the air on the beam path.

The direct signals from the calorimeter were observable by an oscilloscope after 55 meter long 50 ohm coaxial cables with 50 ohm terminators at the end. Figs. 20 a through d are the photographs of the oscilloscope traces of 150 GeV electron induced signals. The wire signal was from the twelfth chamber layer which was at about 9 radiation length almost around the shower maximum for 150 GeV shower. The pad signal was taken from the second longitudinal segment of the pads at  $\eta = 1.475$  or  $\theta = 25.8^\circ$ . It is amusing to see that the wire signal is almost monochromatic even though it represents only about 6 % of the total charge deposited in the whole depth.

The rise time of the signals is about 65 nsec common to the wire and pad signals. This rise time is consistent with the average secondary electron drift time towards the anode wire after being created by the shower which fills the tube cell instantaneously. The tail of the signal is quite different from the anode wire signal to the pad signal because of the large capacitance of the latter.

With such a signal, the pulse height distributions of the total sum in the depth of the wire signals are shown in Figs. 21 a, b, c, and d for 50, 100, 150, and 175 GeV incident electrons, respectively. As mentioned before, these photographs show quite clean electron signals indicating the purity of the beam besides good energy sampling by the calorimeter without large fluctuation.

The hadron shower behaves quite differently. Since this calorimeter represents only 0.9 pion absorption length, 40 % of the incident pions penetrate the calorimeter without interacting with it, and also the rest 60 % do interact but most of the time only partially dump their energies into the calorimeter. This situation is seen in Fig. 22 a in the case of 150 GeV pions.

In the final CDF, the end cap electromagnetic calorimeter will be backed at right behind by a hadron calorimeter which is about 5 pion absorption length thick. A prototype module for the hadron calorimeter was built by LBL group and set up right behind the present module in this test. Fig. 22 b is on-line pulse height distribution of the hadron calorimeter module. The higher pulse height peak corresponds to those pions dumped all their energies into the hadron calorimeter after penetrating the electromagnetic calorimeter without interacting much. Then the addition of the signal must uniquely give the initial pion energies. This expectation is proved to be correct by the fact that the scatterplot, shown in Fig. 22 c, of the electromagnetic calorimeter pulse height vs. hadron calorimeter pulse height is densely populated around an inclined straight line. The peaking of the events at the lowest electromagnetic calorimeter pulse height corresponds to those pions penetrated the electromagnetic calorimeter.

It is important for the present design that the pad signal is exactly proportional to the anode wire signal. Otherwise reading out the pads on only one side of the chambers could result in a worse energy resolution. The scatter plot between the anode signals and the pad signals is shown in Fig. 23. Good proportionality between them indicates that the pads only on one side of the chambers are exactly picking up the total anode wire signal. This will be confirmed again in the later discussion.

The longitudinal electron induced shower development is shown in Fig. 24. It is seen that the depth of the shower maximum deepened almost proportionally to the logarithm of the incident energy as expected.

The lateral shower distributions are shown in Figs. 25 a, b, and c. The second longitudinal segment contains the most of the energy and the third longitudinal segment contains little energy. With increasing the energy, the second segment only increases the contained energy, whereas the first segment remains almost the same. It is also seen that the lateral segmentation both in  $\theta$  and  $\phi$  is adequate with respect to the size of the shower core. It should be noted that the distributions were a little widened because of the signal dispersion over the conductive tube surface which will be much improved in the final construction module by increasing the resistivity to about 100 kohms/sq range. The distribution along the radius will shrink more because the tubes were layed almost parallel to the radius in the present module so that the induced signal tends to flow along the radial direction.

Again difference between pion induced and electron induced signals is observable. The lateral distribution for 100 GeV pions is shown in Fig. 26. The first longitudinal segment does not show a trace but the third segment have some energy deposit.

One of the major objectives of this beam test was to study the effect of the saturation caused by large number of tracks concentrated into a small area in high energy electron induced shower. For this purpose we have tested both the first prototype module and the second prototype module.

Fig. 27 is the plot of the output charge of the first prototype module against the incident electron energies with various combinations of the gas pressure and the high voltage values. Noticeable deviation of the response from straight lines are observable here for charges above about  $2.5 \times 10^4$  ADC counts or 1 nC almost common to all the conditions. This indicates that the saturation is mainly a function of the total charge but not a strong function of the incident energy itself. This is expected from the shower theory which tells us that the shower concentration occurs logarithmically with the energy.

The pressure dependence of the gas gain can be deduced from this graph. The decrease of the charge corresponding to 3 PSI change in the pressure is a factor of  $1/3.6$  between 3 PSI and 6 PSI on gauge. There is another example from MAC prototype calorimeter which changed the gain by a factor of  $1/4.0$  with the pressure change from 5 PSI to 8 PSI on gauge. The former case corresponds to 7.2 % gain change for 1 % change in the absolute gas pressure, or 1 % gain change for 0.14 % absolute pressure change. The MAC calorimeter case corresponds to 8.6 % gain change instead. If we translate this as the gain change due to the density change, the temperature has to be controlled, or at least to be monitored to an accuracy of  $0.38^\circ\text{C}$  in order to suppress the gain change to 1 % level.

The other characteristic of the calorimeter is the high voltage dependence of the gain. In Fig. 28 the total output charge is plotted against the applied high voltage in log scale. The dependence is quite linear with almost identical slope independent of the energy. The slope is a factor of 2.4 increase in the gain for 100 V increment which is equivalent to 0.88 % / V. Therefore the high voltage power supply must have better stability than 1 V for our design because the intrinsic energy resolution goes down to that level at higher energies.

The gain increase substantially deviates from the line above 2.0 kV for all of the energies. This can be understood as the saturation of individual cluster rather than the saturation due to the total charge density.

The response of the second prototype module against the energy is shown in Fig. 29. Saturation is observable for the total charge beyond 0.2 to 0.3 nC. The starting point of the saturation is thus almost a factor of 3 to 5 lower in the total charge than the first prototype module. Since the tube cell dimensions

are exactly the same for these two modules, this is somewhat puzzling for us at this moment.

The logarithmic plot of the total charge against the high voltage shown in Fig. 30 is behaving exactly the same as the one for the first prototype shown in Fig. 28 with regard to its slope and the starting point of the saturation despite the difference in gas pressure.

In the last fall we found that there is an optimum operating voltage for a proportional chamber calorimeter with regard to the energy resolution<sup>7)</sup>. By the present prototype it was again confirmed. The energy resolution for 50 GeV and 100 GeV electrons are plotted against the operating high voltages in Fig. 31. A dip is evidently seen right below the starting point of the saturation. Also it should be noted that the trends for 50 GeV and 100 GeV electrons are identical. It indicates that in this high energy region, electromagnetic shower is essentially a collection of numerous minimum ionizing tracks and the energy resolution is improved by operating the chamber at the edge of the proportional region where larger clusters those consist Landau tail are suppressed by the saturation while the main minimum ionizing peak is still in proportion to the primary ionization.

The best energy resolution is about  $24\% / \sqrt{E}$  at around 1.95 kV.

The dependence of the energy resolution on the energy is again found to be well in proportion to the  $1 / \sqrt{E}$  as shown in Fig. 32. There is no appreciable difference between the energy resolutions obtained by the anode wire and the pads even though, as pointed out before, the pads were only one side of every chamber. This is because the pads are reading out the image signals of the ions created close to the anode wire at the last few stages of the gas multiplication. Since the pairing electrons are almost instantaneously absorbed into the anode wire whereas the ions do not move rapidly because of their almost thousand times slower mobility, it is as if the positive space charges are instantaneously created around the anode wire. Therefore both sides of the conductive plane behind the plastic wall simply shares the whole image signals half and half without statistical fluctuation.

Samely as the first prototype module, the position resolutions were calculated based on the shower centroid measured by the pads and the strips. Here the position is the one projected one-dimensionally to  $r_0$ -axis which is directly comparable with the incident electron position measured by the horizontal beam chambers. The results are plotted in Fig. 33. As observed in the result from the first prototype module in Fig. 15, the best results for the second longitudinal segment of the pad towers. Starting from almost identical value as the first prototype results in the low energy region, it reaches to 1 mm or better above 75 GeV. This will allow us to cut down single and multiple pion background requiring a tight alignment of the shower centroid with the incident point measured by the tracking chamber.

We have already seen in the data that the energy resolution of the pad signal is essentially the same as the one obtained by the anode signal. Further confirmation is necessary whether there is any dependence of the response of the pad signal on the pad size and its incidental capacitance. The summed pad signals were compared with the summed anode wire signals in Fig. 34 taking their ratio scanning the calorimeter polar angles with the beam over the pseudo rapidity range of 1.2 to 2.2. The ratio is flat within  $\pm 3\%$  around the average value 0.35 over  $\eta$  range of 1.27 to 2.07 without any indication of systematic trend. Caution must be taken about this average value ~~of the ratio~~. The small core transformers used to invert the pad signals made sizable sag at the tail which reduced the net observable charge.

As expected from the above result, within the same range of the pseudo rapidity, the energy resolution of the summed pad signals remained the same as shown in Fig. 35. Uniform response was naturally expected when we moved the beam azimuthally keeping the same radius. Fig. 36 shows the response and the energy resolution as a function of azimuthal angle.

Again the effect of the sampling thickness on the energy resolution was studied artificially sparsing the sampled layers in off-line analysis. All the results in Fig. 37 are well fitted by  $1/\sqrt{E}$  dependence. Fig. 38 summarizes the results and in all cases it is represented by a single formula again

$$\sigma_E/E = k \sqrt{t/E} \%$$

with  $k = 31$  consistently with the result from the first prototype module as mentioned before.

The same kind of software manipulation was done to study the effect of the dummy material in front of the sampled layers. The wall of the gas vessel and an aluminum holder contributed about one radiation length and then the signals from the front layers were ignored layer by layer in the summation to obtain the total charge. The results plotted in Fig. 39 show that such dummy material does not affect the energy resolution up to 2 to 3 radiation length at higher energies.

Further study was done to see the effect of the energy leakage, or finite depth of the calorimeter on the energy resolution. Signals of the chambers at the last part of the calorimeter were ignored in the software one by one. The graph shown in Fig. 40 clearly indicate that 20 radiation length is enough for the present energy range.

Finally, the main role of the calorimeter is not only to measure the electron energy, but to identify electrons against hadron background. For those incident hadrons which develop hadronic shower, the discrimination is essentially based on the large difference between the radiation length and the hadronic absorption length of lead absorber. The present calorimeter is about 25 radiation length thick but only contribute 0.9 hadronic absorption length. Therefore, electrons develop the shower rapidly and exhaust all the energy within the calorimeter, whereas hadrons penetrate in 40 % of the cases and the rest 60 % barely develop the hadronic shower. Therefore it is in principle possible to distinguish those hadrons. What remain indistinguishable are those pions which develop electromagnetic shower at the early stages of the interactions via charge exchange interactions. Therefore ordinary strategy was to segment the calorimeter longitudinally at the shallowest possible part just diminish the probability of the charge exchange interactions within it. The situation is different in the higher energy region we are dealing with. Charge exchange cross section<sup>8)</sup> decreases logarithmically with the energy. For example at 20 GeV it is almost two orders of magnitude smaller than the total pion absorption cross section. Then the optimum way of rejecting pions is not necessary to examine the shallowest possible part of the calorimeter for the early part of the energy deposit in it.

Another condition for CDF which is quite different from ordinary fixed target experiment is that the momentum measurement significantly deteriorates in the lower angles because the incident particles do not go through full depth of the tracking chamber layers. Therefore the requirement that the  $E/P$  ratio be close to 1 for electrons, which is the most effective cut for ordinary experiment, is not necessarily applicable to the present end cap calorimeter.

In order to simulate such condition, we have studied the rejection of those pions which have the same or larger energy than the interested electrons varying both the electron and hadron energies.

The algorithm for the discrimination was one of the various combinations of the following requirements to the electron candidates;

- 1) energy deposit in the first segment be within a certain range,
- 2) energy deposit in the third segment be smaller than a certain upper bound,
- 3) r.m.s. spread of Gaussian fitted lateral shower distribution in the second segment be within certain range.

In order to maintain the generality of these cuts independent of the energy, the energy deposits in the first and the third segments were normalized by the observed total energy deposit. Fig. 41 a shows the resulted efficiencies for pions against the electron efficiencies for the case that 100 GeV pions were compared with the electrons of the same energy. For each pion, the cuts on the parameters used were done with the same number of units of r.m.s. spread of each distribution so that the overall loss of the electron efficiency was minimal.

The case that the pion energy is a factor of 2 higher than the electron energy is shown in Fig. 41 b for the electron energy of 50 GeV. In either of the above cases the combination of the above three cuts resulted in a factor of about  $1.5 \times 10^{-2}$  in the pion efficiency with 80 % or better electron efficiency.

It should be stressed again that this is a rejection without imposing any cut on the total energy. If one tries to calculate the realistic background faked by the higher energy pions, it must be properly binned in the electron like event energy which will much improve the above quoted rejection factor. For example, if we take a bin width of about 5 times the observed electron energy resolution, the pion efficiency is well below  $2 \times 10^{-3}$  independent of the pion and electron energy combination.

The pion rejection factors for the case that backing hadron calorimeter signal is used in the algorithm are almost an order of magnitude better. The additional requirement for electrons is then

- 4) the energy deposit in the hadron calorimeter is smaller than a certain upper bound.

Again the energy deposit in the hadron calorimeter was normalized by the observed total energy in the combined system.

In order to verify the generality of such cuts irrespective of the energies, the pion efficiencies are plotted in Fig. 42 against the ratio of the energy of the pions to the energy of the electrons in the examined combination. Within the present energy range of the pions between 75 and 150 GeV the results seem to be stable for  $E_e/E_\pi$  ratio between 0.25 and 1.

## CONCLUSIONS

- 1) We have been successful in fabricating the conductive plastic tubes of proper quality, i.e. good dimensional tolerance and the resistivity tolerance. The cell inner dimension was  $(7 \pm .1) \times (10 \pm .1) \text{ (mm)}^2$  and the resistivity was  $30 \pm 10 \text{ kohms/square}$ .
- 2) No significant problem has been seen in the operation of the two generations of prototype modules. There was no irregular break down. No noticeable damage on the tube was detected when tubes were purposely let break down. No noticeable outgassing was observed.
- 3) The mechanical structure chosen here in which the conductive plastic tubes were sandwiched with two G-10 boards was quite rugged. It is a quite suitable way to maintain the uniformity of the gap thickness as well as the flatness, and also it is free from thermal distortion

- and thermal change of the dimensions.
- 4) Using the conductive plastic tubes as the proportional tube elements, the pick-up electrodes can be on the outside allowing one to segment them into any fine pattern.
  - 5) It was observed that the best energy resolution was obtained at the higher voltage end of the proportional region consistently with the idea of saturated avalanche mode.
  - 6) Good energy resolution was obtained. The optimum value was  $29 \sqrt{t/E} \%$  with the second prototype module.
  - 7) The energy resolution obtained by the pads was identical to the one obtained by the anode wires even though the pads were only on one side of every chamber.
  - 8) Pad response was quite uniform, independent of the pad size, with regard to the total pulse height, The energy resolution, and the position resolution.
  - 9) The signal rise time was identical for the pads and the anode wires. The observed value 65 nsec is consistent with the average electron transit time in a cell.
  - 10) Good position resolution was obtained based upon the pad and the strip signal. The second longitudinal segment of the pad tower was the best in this respect and resolutions of 1 mm or better was achieved for energies above 75 GeV.
  - 11) Without using E/P cut, the pion rejection was about  $2 \times 10^{-2}$  by the electromagnetic calorimeter alone. With additional information from the backing hadron calorimeter it was improved to  $2 \times 10^{-3}$  independent of the  $E_0/E_\pi$  ratio for the compared combination.

#### REFERENCES

- 1) Design Report for the Fermilab Collider Detector Facility ( CDF ) 1981.
- 2) T. Katsura et al., Nucl Inst Meth 105 (1972) 245.  
R.L.Anderson et al., IEEE Trans Nucl Sci NS-25 (1978) 340.  
R.L.Walker et al., Fermilab Internal Report CDF-95 (1981).  
M.Atac et al., IEEE Trans Nucl Sci NS-28 (1981) 500.  
J.J.Mueller et al., CBX 81-28 (1981).  
H.Tycho et al., UCLA Preprint.
- 3) M.Atac, IEEE Trans Nucl Sci NS-28 (1981) 492.
- 4) F.Paige, BNL-27066, Invited talk at Topical Workshop on the Production New Particles in Super High Energy Collisions, Madison, Wisconsin, 1979.
- 5) M.Atac et al., IEEE Trans Nucl Sci NS-29 (1982) 368.  
Y.Hayashide et al., To be published in Nucl Inst Meth.
- 6) Y.Hayashide et al., To be published in IEEE Trans Nucl Sci.
- 7) M.Atac et al., Nucl Inst Meth 205 (1983) 113.
- 8) V.Flaminio et al., Compilation of Cross-Sections.I  $\pi^-$  and  $\pi^+$  Induced Reactions.

## TABLE CAPTIONS

Table 1: Comparison of the parameters of the first and second prototype calorimeter modules for CDF end cap electromagnetic calorimeter based on conductive plastic proportional tubes.

Table 2: Configuration of the first prototype module layers.

Table 3: Configuration of the second prototype module layers.

TABLE 1

-13-

|                          | PROTOTYPE I   | PROTOTYPE II  |
|--------------------------|---|---|
| BUILT                    | Spring 1981   | Spring 1982   |
| LAYER STRUCTURE          | Pb Sheet - G 10 Panel - Conductive Plastic Tube Array - G 10-Panel Sandwich |   |
| CONDUCTIVE PLASTIC TUBES |   |   |
| CELL ID                  | 7 mm x 10 mm  |   |
| WALL THICKNESS           | 1.5 mm  | 0.8 mm  |
| ANODE WIRE               | 50 um Gold Plated Tungsten Wire   |   |
| SHAPE                    | Cylindrical   | Cylindrical   |
| OUTER RADIUS             | 50 cm   | 140 cm  |
| INNER RADIUS             | 8 cm  | $\eta = 2.3$ cone ( $r=38 - 49$ cm)                               |
| AZIMUTHAL APERTURE       | 90°   | 30°   |
| PAD/STRIP TOWER          | Cylindrical   | Conical   |
|                          | $r - \phi$  | $\eta - \phi$   |
| CABLING                  | RG 174  | Short Flat Cable<br>+ 280 n sec RG 58 U<br>equivalent 50 ohm Coax |
| ELECTRONICS              | Integrator<br>right next to Module  | LRS 2285A 15 bit ADC  |
| LEAD SHEET               | 2 mm around shower max<br>6 mm Front, 8 mm Rear                             | 3 mm  |
| TOTAL THICKNESS          | 20.3 X <sub>0</sub>   | 22.4 X <sub>0</sub> x 1/cos $\theta$                              |
| GAS                      | Argon - Ethane 50-50% ( Ethylalcohol 1.4 % )                                |   |
| BEAM TEST                | M-5: 10 - 46 GeV (1981)<br>M-4: 25 - 175 GeV (1982)                         | M-4: 25 - 175 GeV (1982)  |

TABLE 2

## CONFIGURATION OF THE FIRST END CAP E.M. CALORIMETER PROTOTYPE MODULE

| SEGMENT NUMBER | LAYER NUMBER | TYPE OF CHAMBER | LEAD PLATE THICKNESS | RADIATION LENGTH | STRIP CHAMBER DEPTH |
|----------------|--------------|-----------------|----------------------|------------------|---------------------|
| I              | 1            | Pads            | 8 mm                 |                  |                     |
|                | 2            | Pads            | 4 mm                 | 2.3 X            |                     |
| II             | 3            | Pads            | 2 mm                 |                  |                     |
|                | 4            | Strips-1        |                      |                  | 3.2 X               |
|                | 5 - 7        | Pads            |                      |                  |                     |
|                | 8            | Strips-2        |                      |                  | 4.9 X               |
|                | 9 - 15       | Pads            |                      |                  |                     |
|                | 16           | Strips-3        |                      |                  | 8.2 X               |
|                | 17 - 24      | Pads            |                      |                  |                     |
| III            | 25           | Strips-4        |                      |                  | 12.0 X              |
|                | 26 - 28      | Pads            | 6 mm                 |                  |                     |
|                | 29           | Strips-5        |                      | 8.2 X            | 16.7 X              |
| TOTAL          |              |                 |                      | 20.3 X           |                     |

|              |    |         |           |    |
|--------------|----|---------|-----------|----|
| Vessel Wall  | Fe | 1/2 in. | 0.722 rad | 1. |
| Holder Plate | Al | 1 in.   | 0.285 rad | 1. |

TOTAL 22.40 rad l.

# FIGURE CAPTIONS

Fig. 1: Cross sectional view of the end cap electromagnetic calorimeter for the Collider Detector at Fermilab. Polar angles are shown by lines at every  $5^\circ$  with respect to the center of the interaction region. Shadow around each line indicates the smearing of the track within the calorimeter due to the finite length of the interaction region. R.m.s. bunch length of each beam was taken as 40 cm. R.m.s. length of the interaction region must be  $1/\sqrt{2}$  of the bunch length and is 28.3 cm. The cross sectional view of the radial segmentation is shown by broken lines.

Fig. 2: Pt distribution of the differential cross sections for positive and negative leptons from leptonic decays of  $W^\pm$ . The curves were calculated by F. Page's program<sup>4)</sup> which takes only Born terms with correcting the quark structure functions for QCD effects. Solid lines are for  $\ell^+$  and the broken lines are for  $\ell^-$  in proton forward hemisphere. Prediction by Field-Feynman-Fox at  $90^\circ$  is also shown by open circles.

Fig. 3: Laboratory momentum spectrum of  $\ell^\pm$  from  $W^\pm$  decay in proton forward hemisphere.

Fig. 4: Layout of the pads to be etched on copper clad G-10 boards on one side of every chamber layer.

Fig. 5: Sketch of a  $30^\circ$ -sector layer composition. A plastic proportional tube array is stacked with two G-10 boards with appropriately etched copper plating. One side is always pads facing the tube array and the opposite side is mostly ground plane other than those with  $\theta$ - or  $\phi$ -strips on the chambers around the shower maximum. The upper G-10 panel in this figure is therefore merely to illustrate how the signal strip lines on the back of the pad panels are lead to the edge card connectors at the outer radius of the panel.

Fig. 6: Cross sectional dimensions of conductive plastic tubes.

Fig. 7: Pulse height spectrum of  $Fe^{55}$  observed by a proportional tube made of conductive plastic tube strung with 50  $\mu m$  gold plated tungsten wire as the anode.

Fig. 8: Outside pickup electrode patterns; a: Pads., b:  $\theta$ -strips., c:  $\phi$ -strips.

Fig. 9: Sketch of a  $90^\circ$ -sector layer for the first prototype module.

Fig. 10: Longitudinal development of the shower for electrons and hadrons.

Fig. 11: Charge collected on anode wires and cathode pick-up electrodes plotted against the incident electron energies. The charge for the cathode electrodes is the sum of the signals on pads,  $\theta$ -strips, and  $\phi$ -strips.

Fig. 12: The energy resolutions for the anode signal and the cathode signal are plotted against  $1/\sqrt{E}$ .

Fig.13: Energy resolutions vs.  $1/\sqrt{E}$  for the coarser sampling thicknesses reproduced by software manipulation.

Fig.14: Event-by-event deviation of the lateral shower centroid from the incident point measured by the beam pwc's.

Fig.15: R.m.s. deviation of the lateral shower centroid from the real incident point measured by the beam pwc's in front of the calorimeter.

Fig.16: Sketch of the second prototype module. Tube array was parallel to one side of the radial edge.

Fig.17: Layout of the cathode pick-up electrodes. a: pads, b:  $\theta$ -strips, c:  $\varphi$ -strips.

Fig.18: Connections and cabling of the anode and cathode signals.

Fig.19: Fermilab M-4 beam line arrangement.

Fig.20: Oscilloscope traces of the 150 GeV electron shower signals from anode wires and pads. The wire signal was taken from the twelfth chamber layer which was about at the shower maximum, and the pad signal was from the second longitudinal segment of the pads at  $\eta = 1.475$ , or  $\theta = 25.8^\circ$ . The signals were brought directly to an oscilloscope by 55 meter long, 280 nsec in delay, 50 ohm RG 58/U equivalent coaxial cables and terminated by 50 ohms. Pad signals are inverted in these photographs. Vertical scale is 5 mV / div. a: 50 nsec / div, b: 100 nsec / div, c: 200 nsec / div, d: 500 nsec / div.

Fig.21: On-line histograms of the pulse height distributions at 1.8 kV. a: 50 GeV electrons, b: 100 GeV electrons, c: 150 GeV electrons, d: 175 GeV electrons.

Fig.22: Pulse height distributions of 150 GeV hadrons. a: Energy deposit into the present electromagnetic calorimeter, b: energy deposit into the backing prototype hadron calorimeter, c: scatter plot between the energy deposits into the above two calorimeters.

Fig.23: Scatter plot of the summed pad signals vs. the summed anode wire signals for 25, 50, and 75 GeV electrons.

Fig.24: Longitudinal development of electron induced shower.

Fig.25: Lateral distribution of electron induced shower. a: 50 GeV, b: 100 GeV, c: 150 GeV.

Fig.26: Lateral distribution of 100 GeV hadron induced shower.

Fig.27: Response of the first prototype module against the incident electron energies for various values of the gas pressure and the high voltage.

Fig.28: Logarithmic dependence of the total charge from the first prototype module on the applied high voltage with the incident electron energies as the parameters.

Fig.29: Response of the second prototype module against the incident electron energies with varying the applied high voltage.

Fig.30: Logarithmic plot of the total charge from the second prototype module against the applied high voltage for 100 GeV electrons.

Fig.31: The high voltage dependence of the energy resolution for 50 GeV and 100 GeV electrons.

Fig.32: Energy resolution plotted against  $1 / \sqrt{E}$ .

Fig.33: Position resolution perpendicular to the beam in radial plane.

Fig.34: Ratio of the summed pad signals to the summed anode wire signals over pseudo rapidity range from 1.2 to 2.2.

Fig.35: Energy resolution measured by the pads and the anode wires over pseudo rapidity range from 1.2 to 2.2.

Fig.36: Total charge and the energy resolution measured by the pads and the anode wires moving the beam azimuthally keeping the same value of pseudo rapidity.  $\phi = 15^\circ$  corresponds to the middle of 30-sector.

Fig.37: Energy resolutions with different sampling thicknesses. The sampled layers were artificially sparsed in the off-line analysis.

Fig.38: Effect of the sampling thickness on the energy resolution.

Fig.39: Effect of dummy material in front of the sampled layers. Signals from the front layers were layer by layer ignored in the summation to obtain the total charge in software.

Fig.40: Effect of the shower leakage from the back of the calorimeter

Fig.41: Pion rejection factor plotted against electron efficiencies. a: 100 GeV pions against 100 GeV electrons, b: 100 GeV pions against 50 GeV electrons.

Fig.42: Pion rejection factor plotted against  $E_e/E_\pi$  where  $E_e$  is the interested electron energy and  $E_\pi$  is the background pion energy.

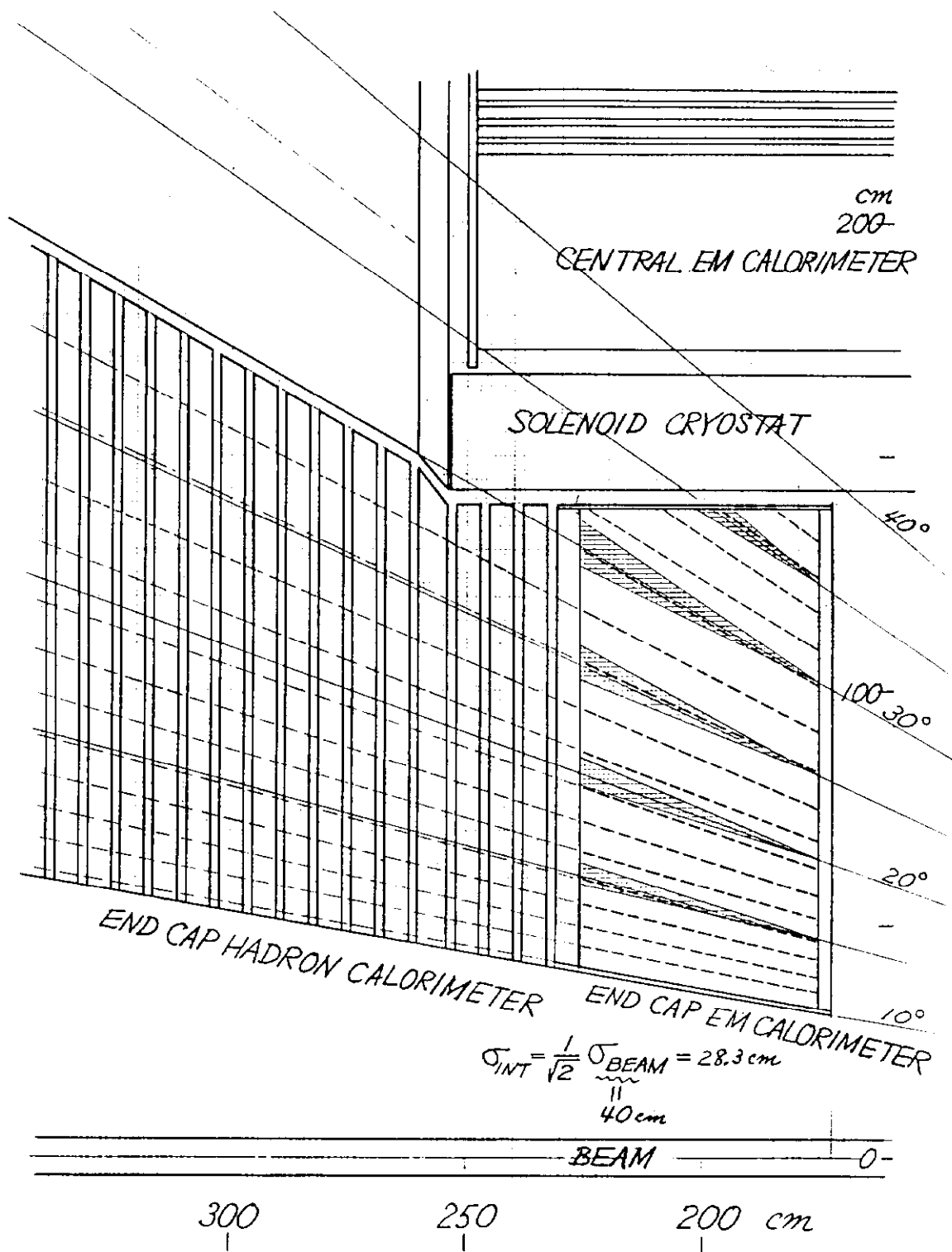


Fig. 1

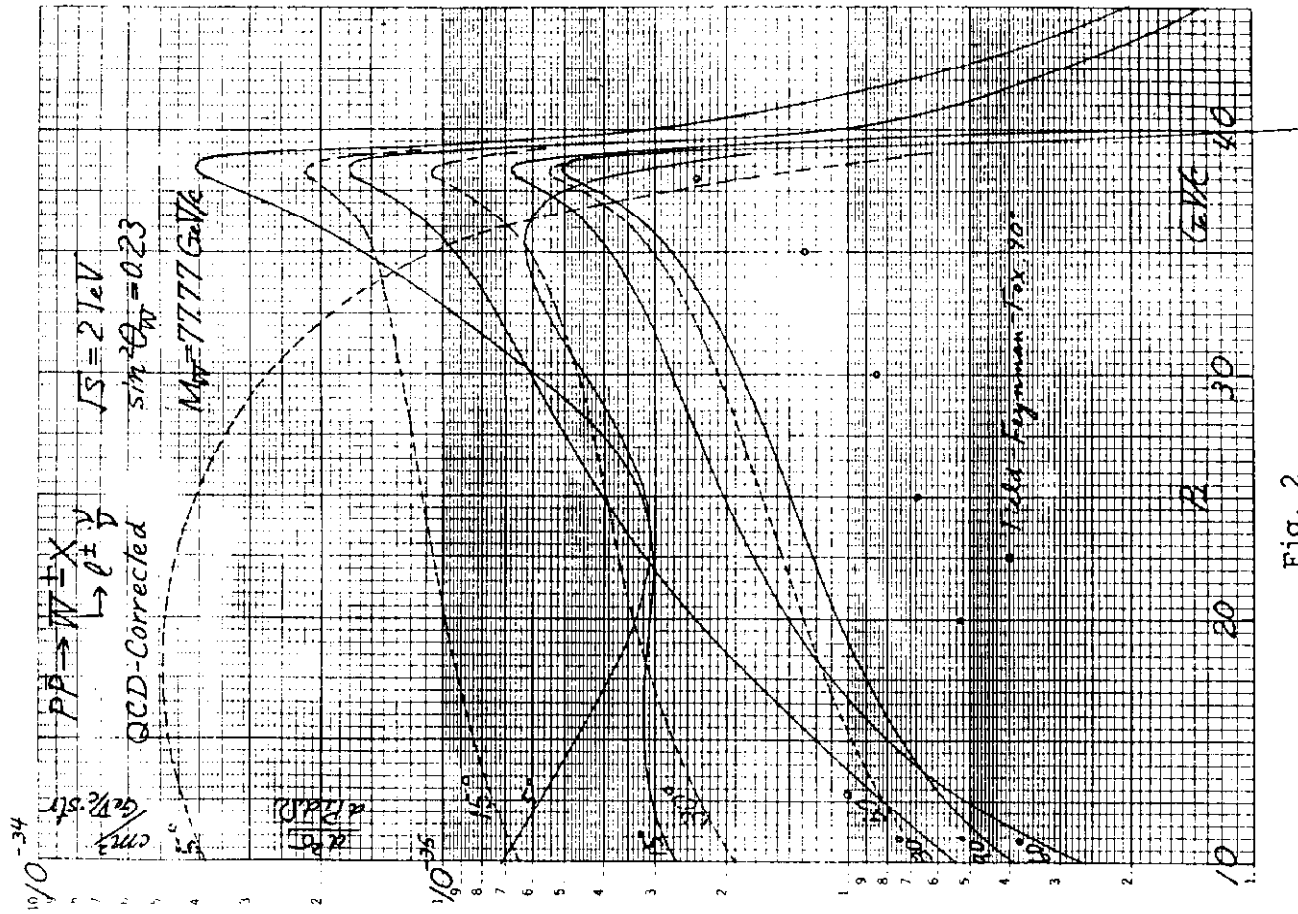


Fig. 2

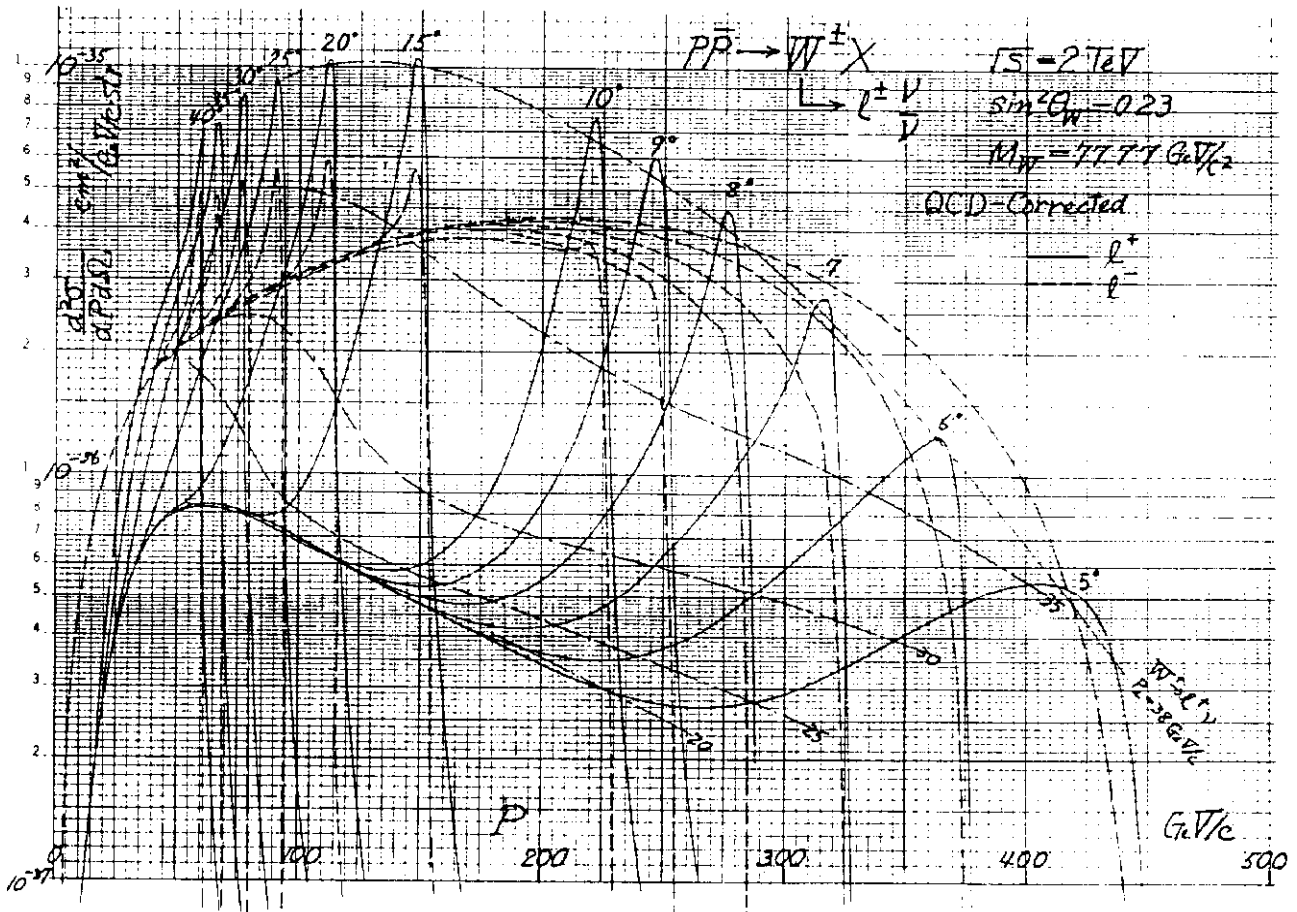


Fig. 3

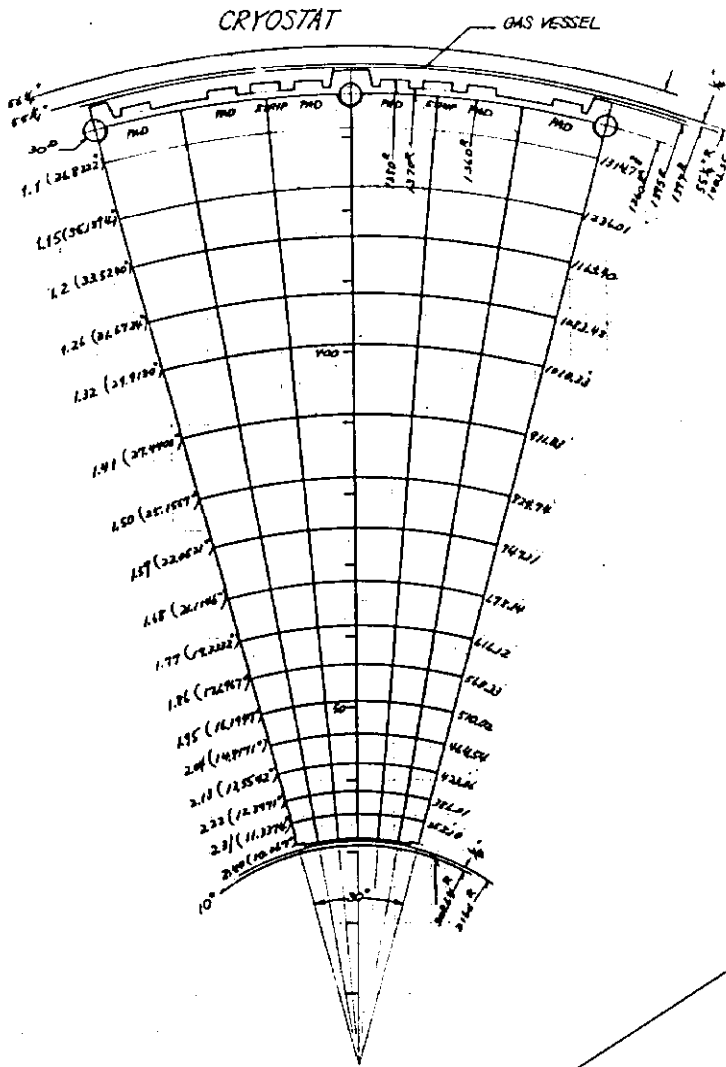


Fig. 4

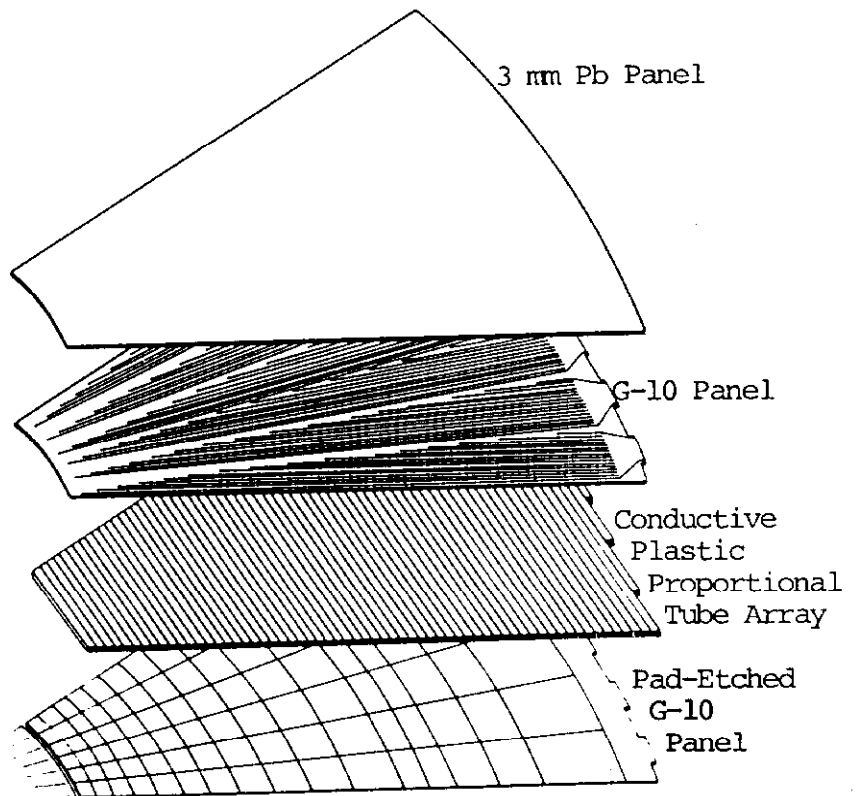


Fig. 5

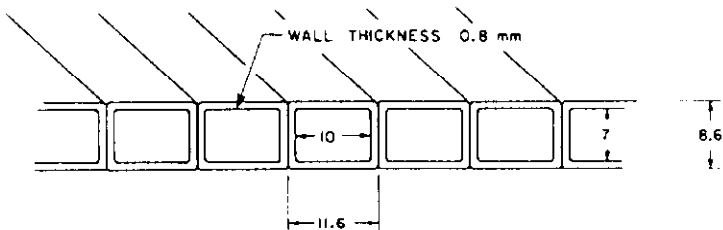
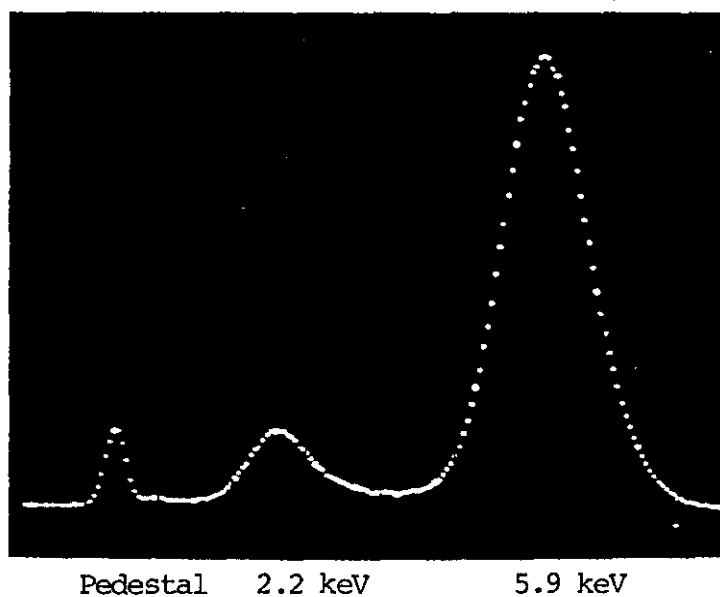


Fig. 6



$\text{Fe}^{55}$  : Irradiated through the wall (0.8 mm thick) .

1.9 kV

Ar-Ethane 50%-50% (Ethylalcohol 1.4%)

50  $\mu\text{m}$  Gold Plated Tungsten Wire

$7 \times 10 \text{ (mm)}^2$  Cell

Fig. 7

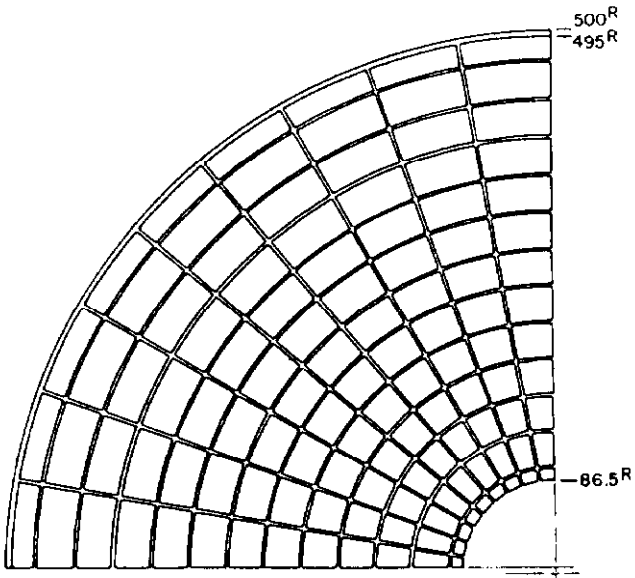


Fig. 8 a

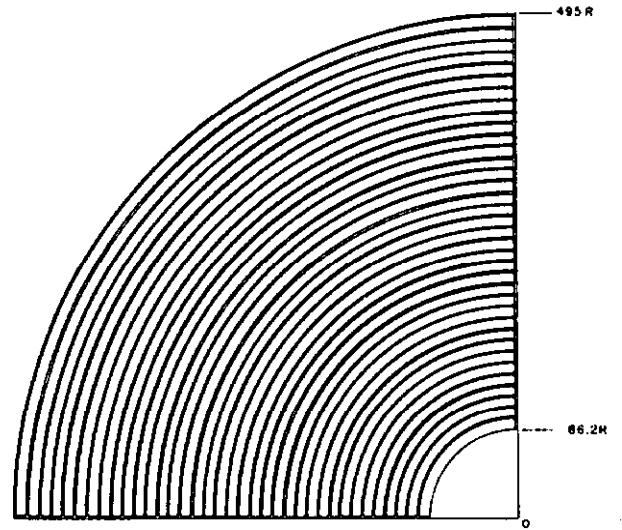


Fig. 8 b

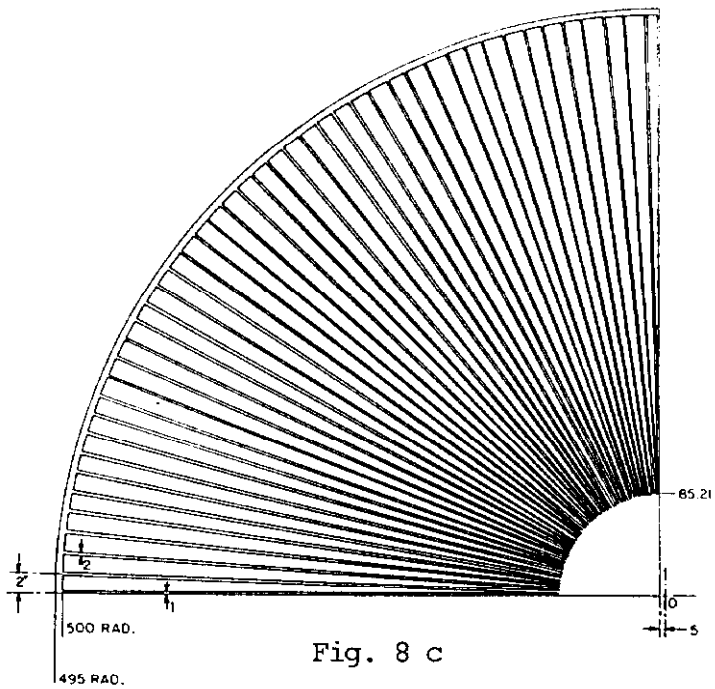


Fig. 8 c

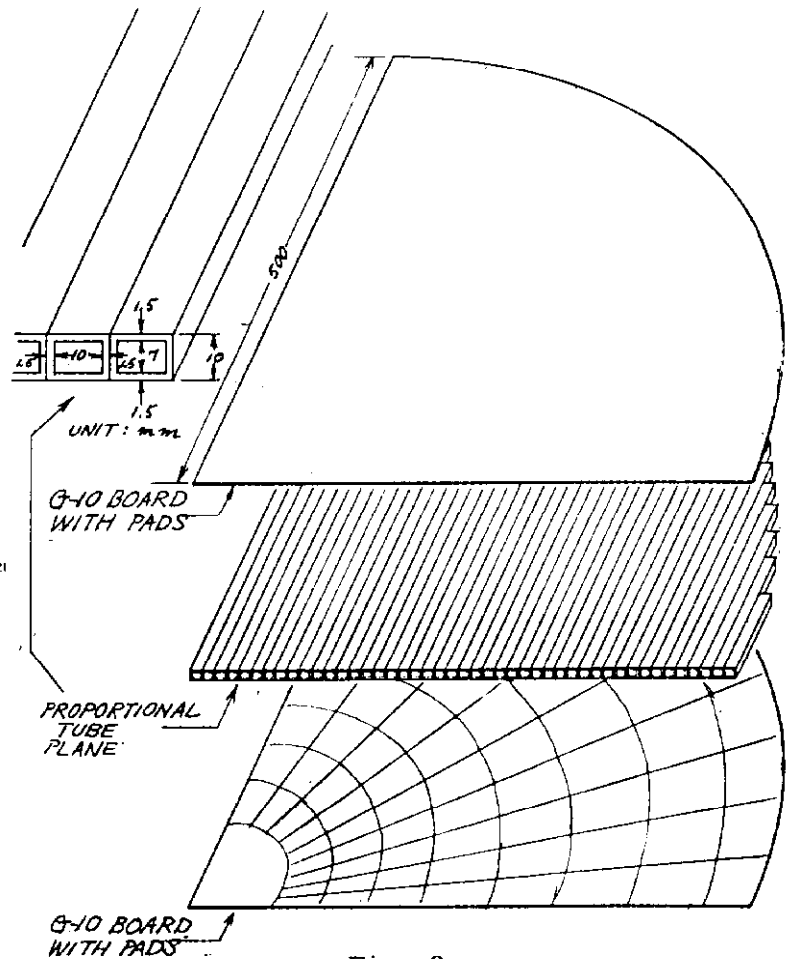


Fig. 9

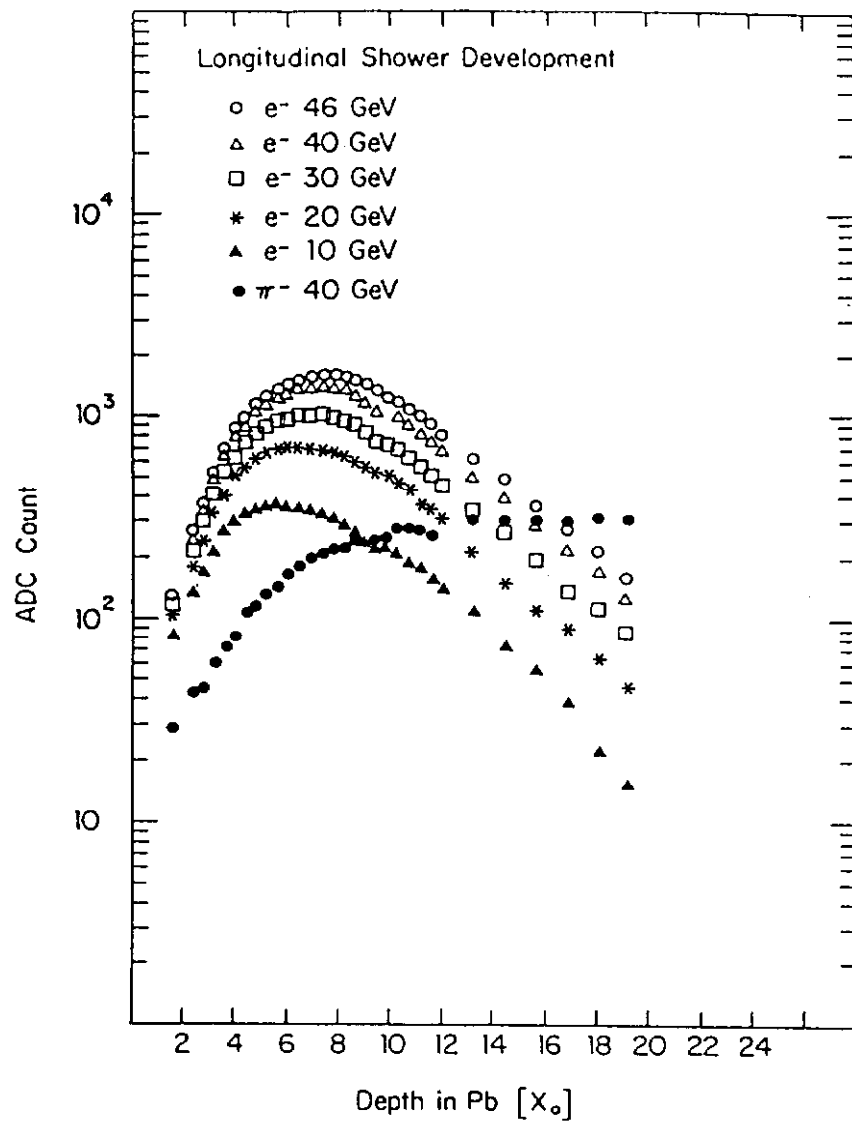


Fig. 10

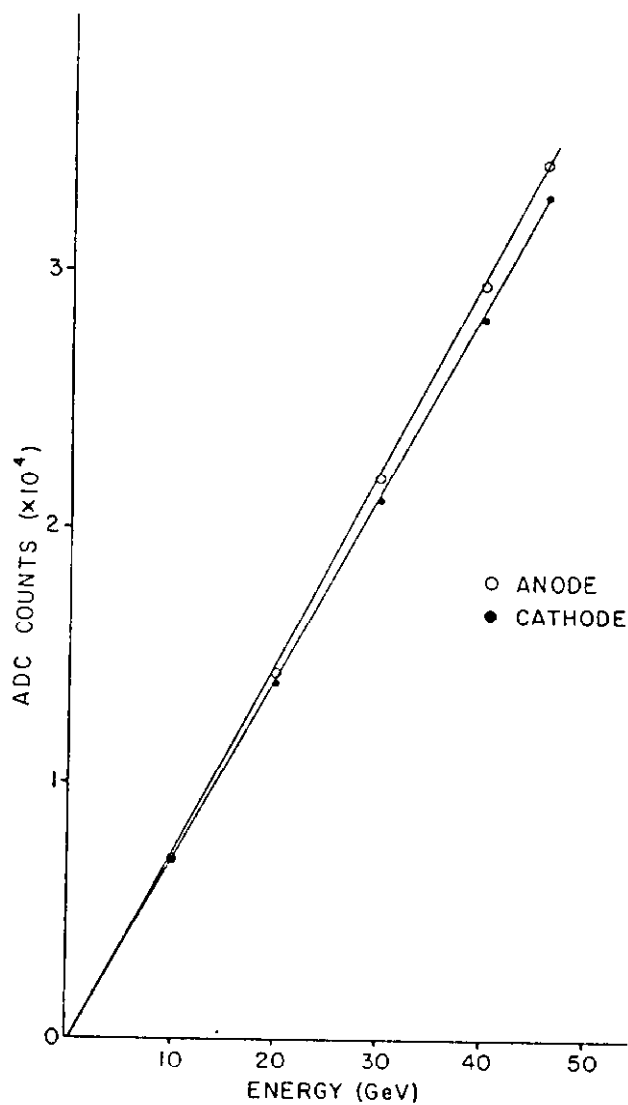


Fig. 11

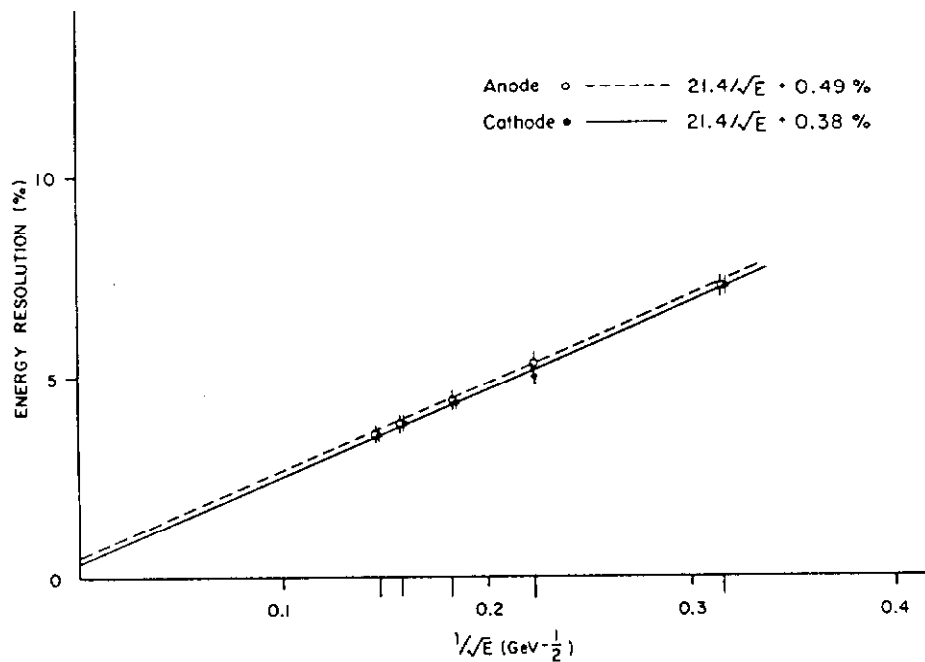


Fig. 12

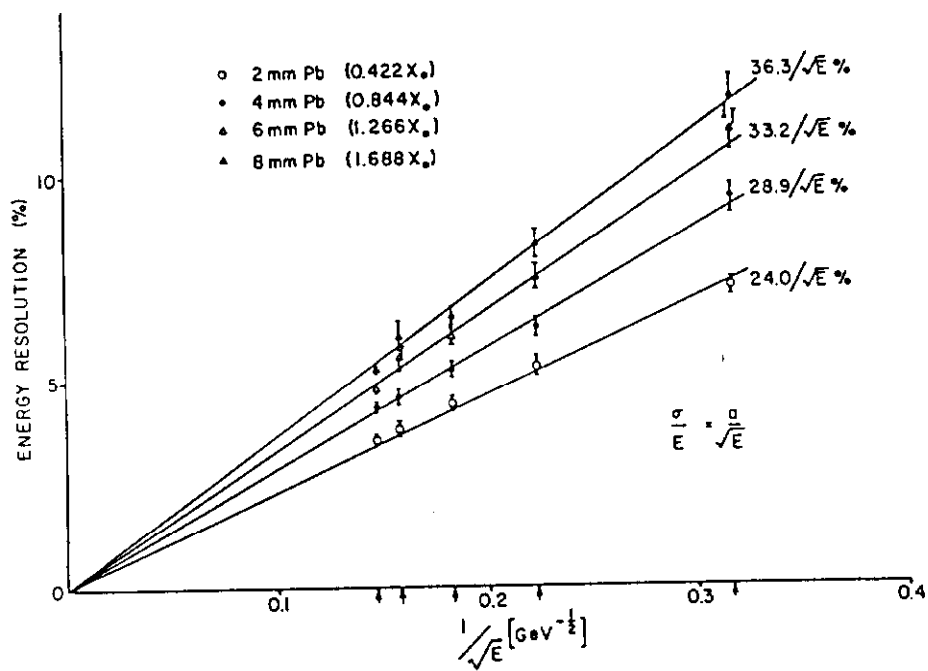


Fig. 13

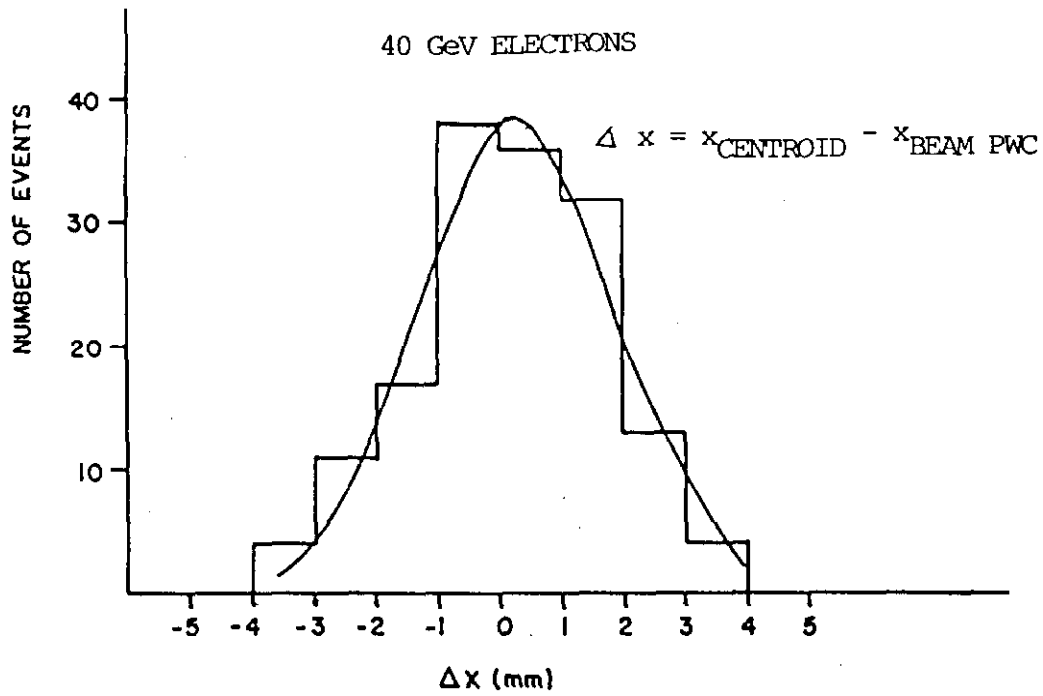


Fig. 14

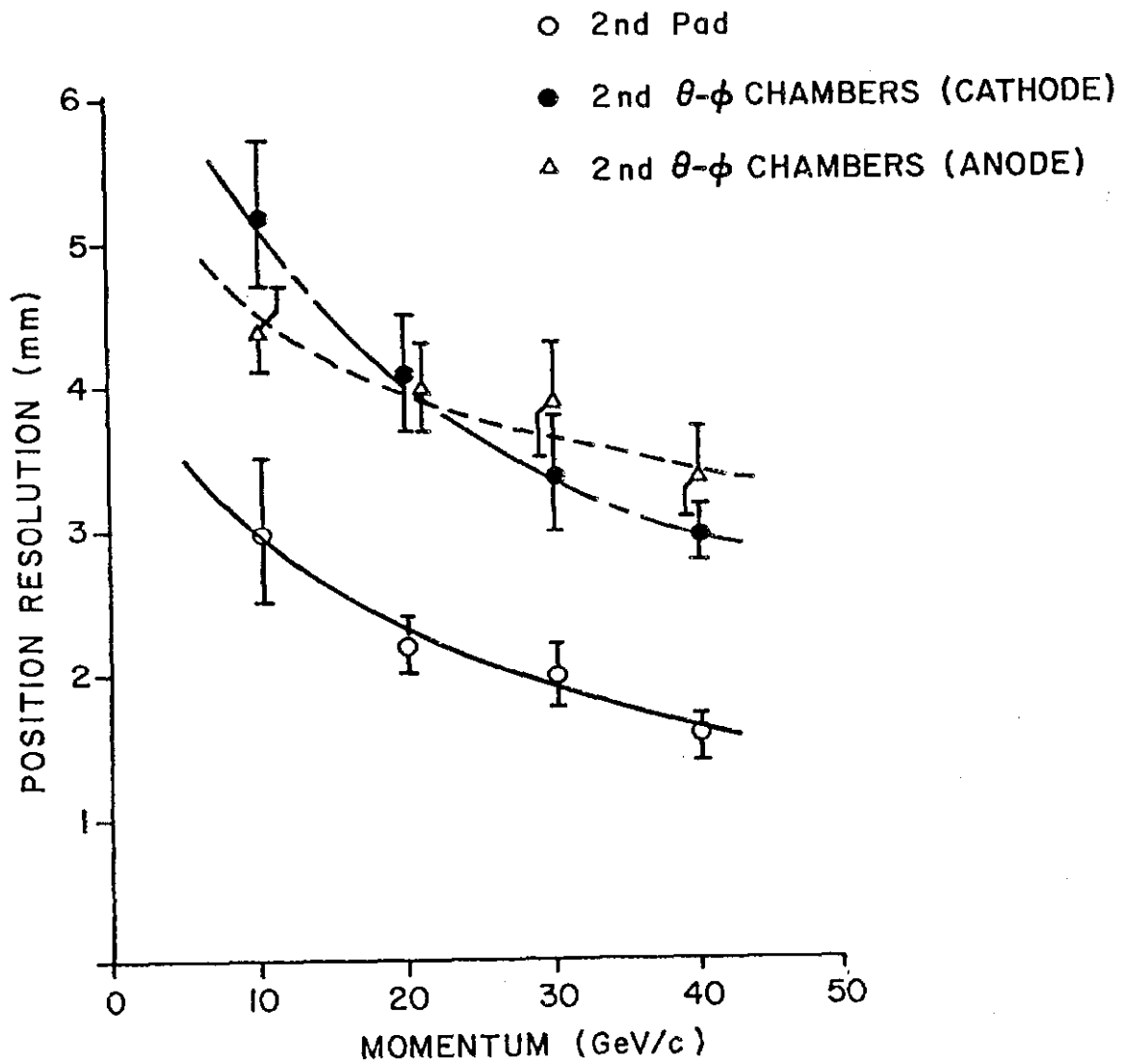


Fig. 15

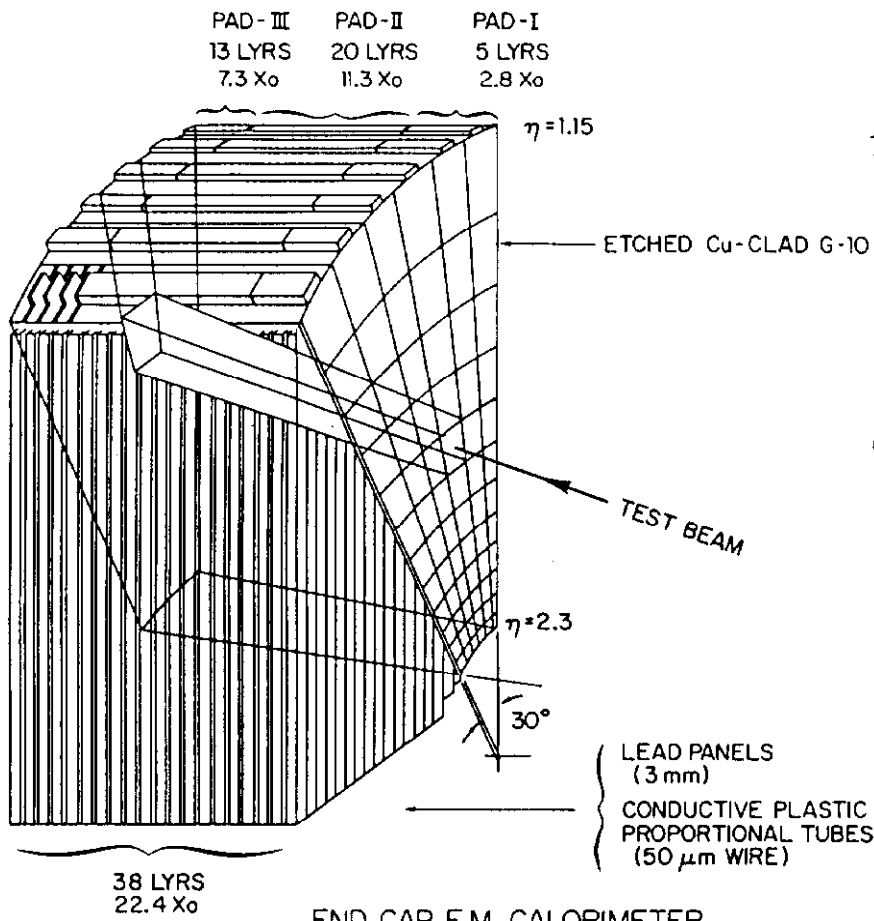


Fig. 16

END CAP E.M. CALORIMETER  
PROTOTYPE MODULE

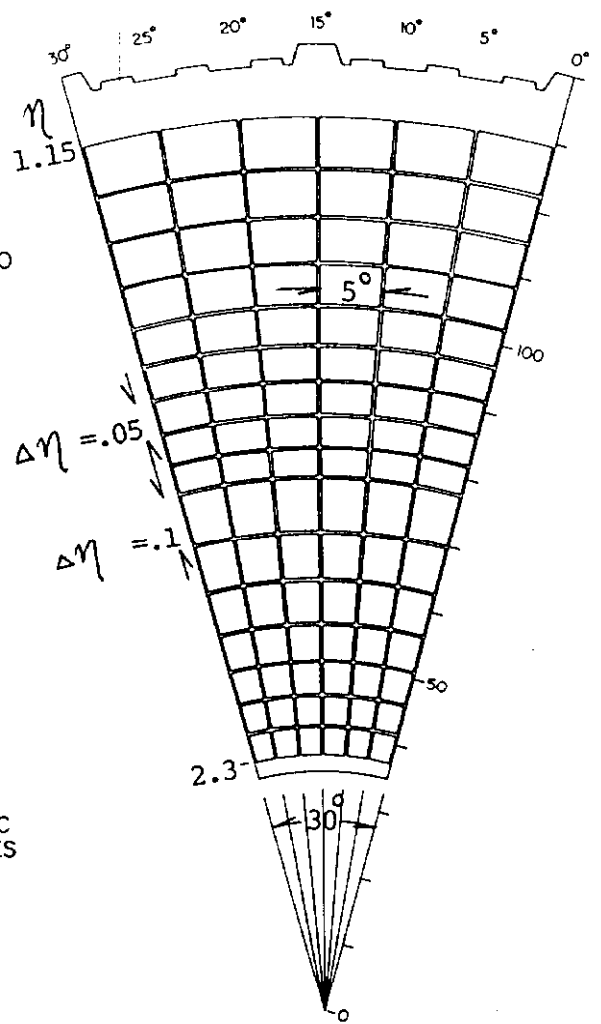


Fig. 17 a

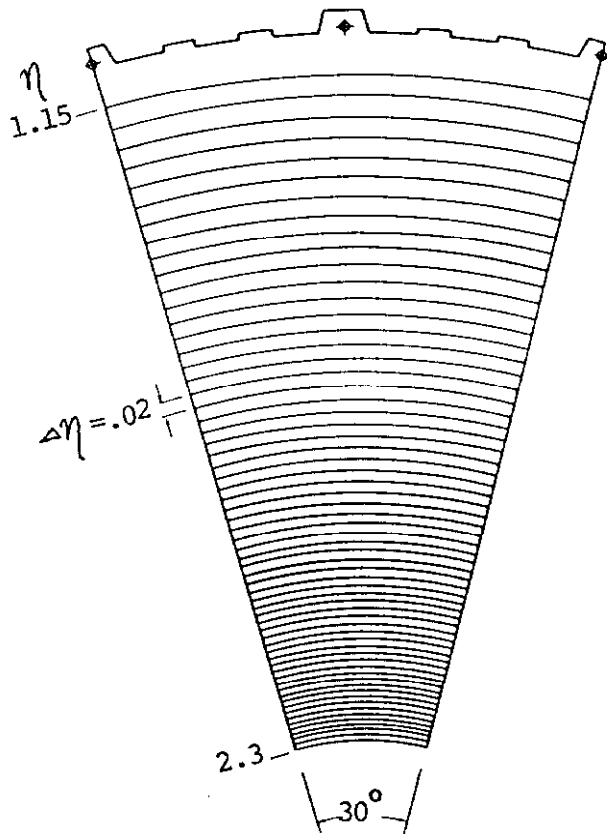


Fig. 17 b

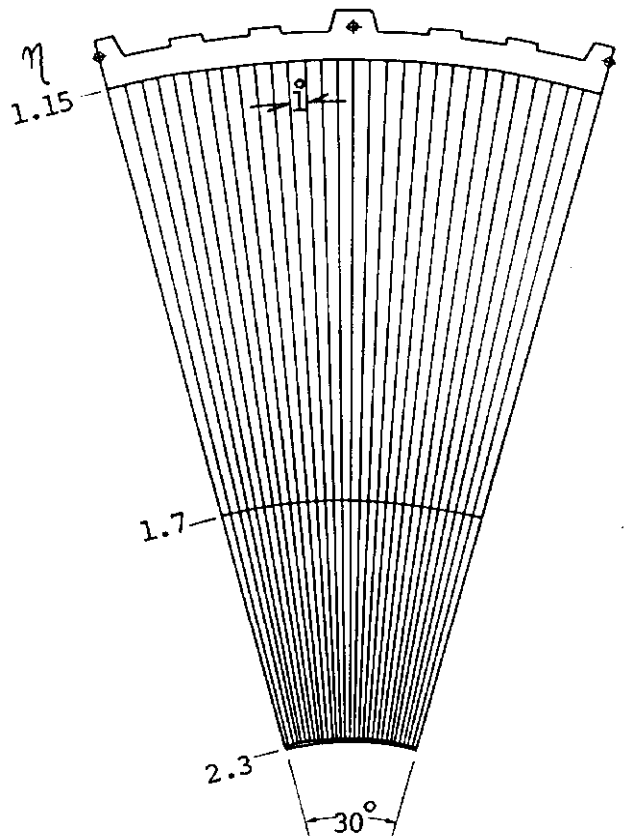


Fig. 17 c



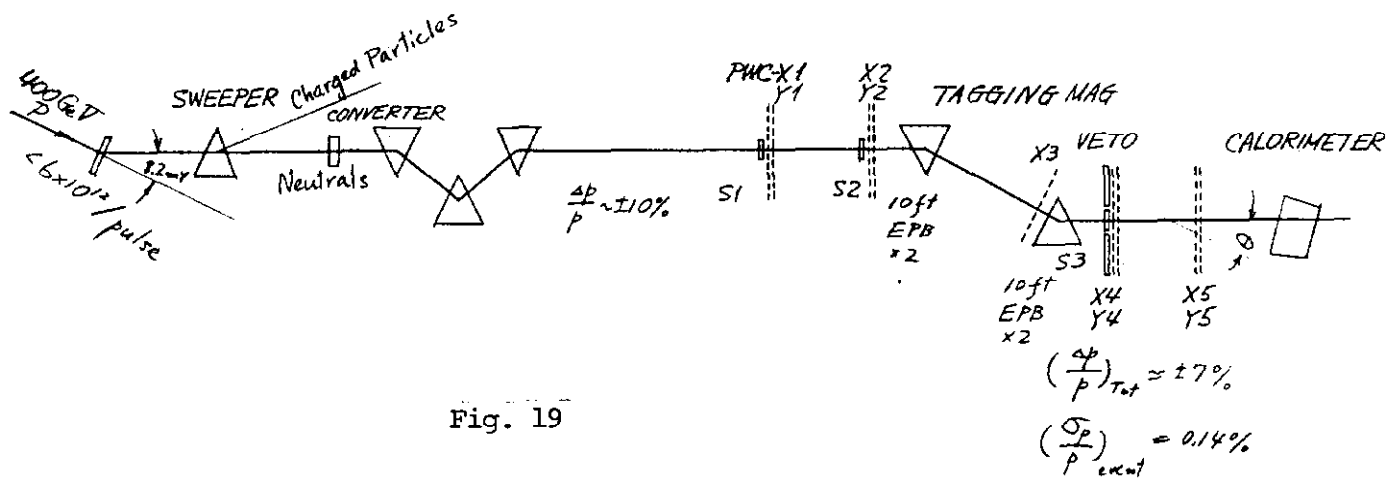


Fig. 19

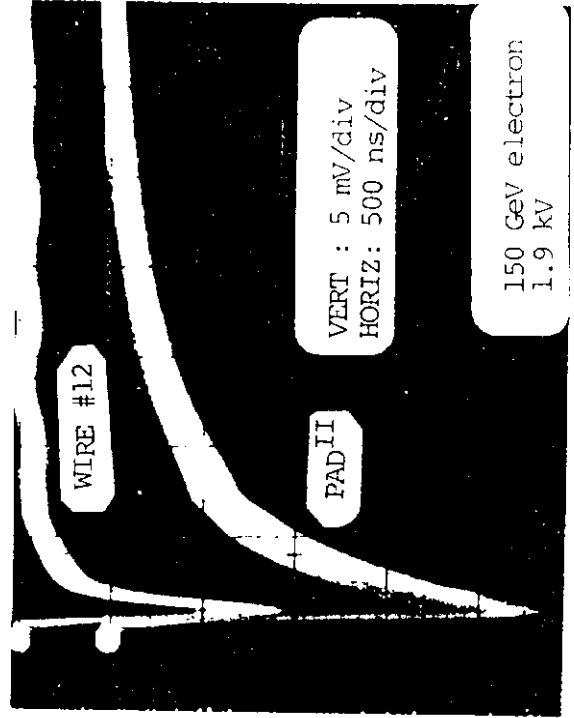
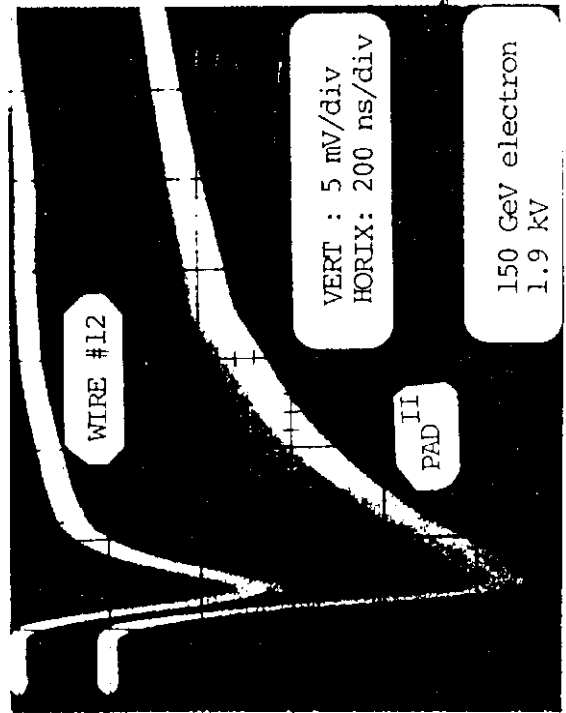
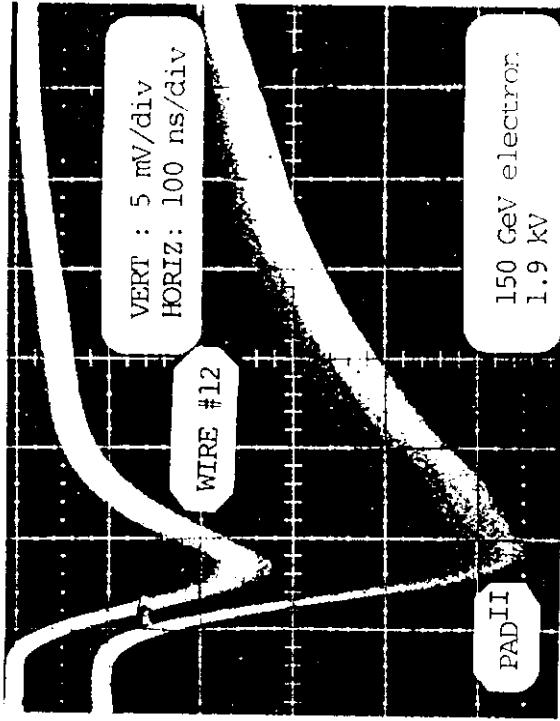
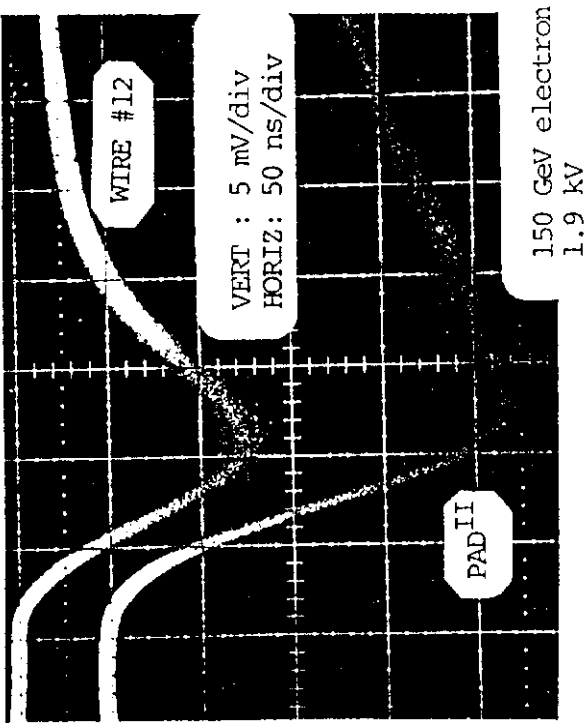
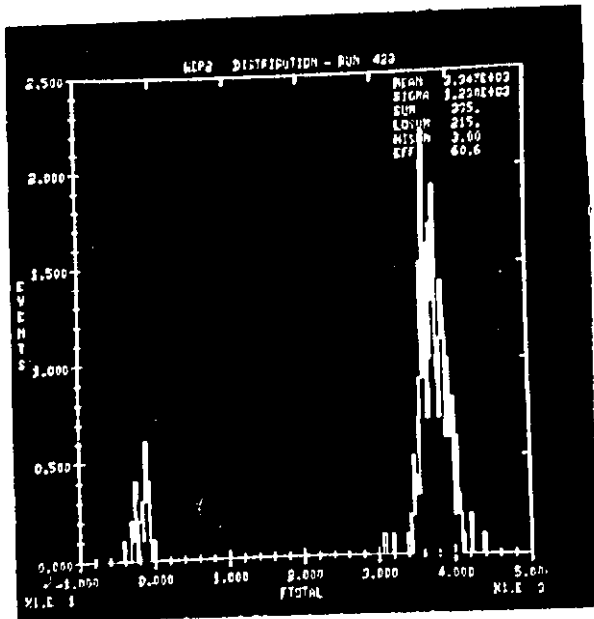
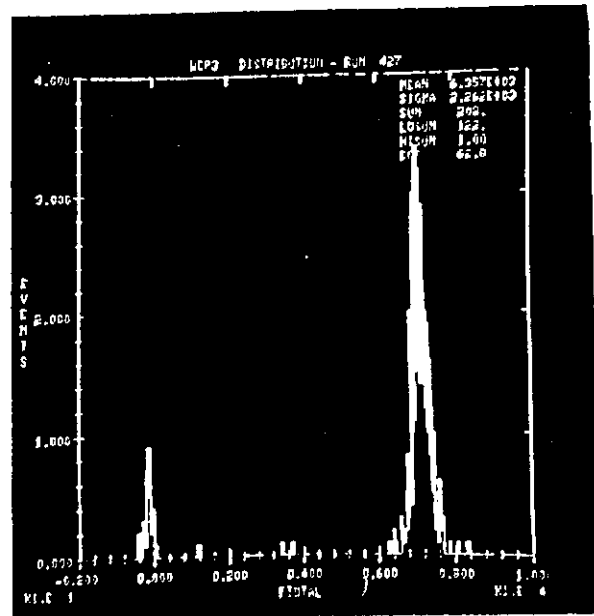


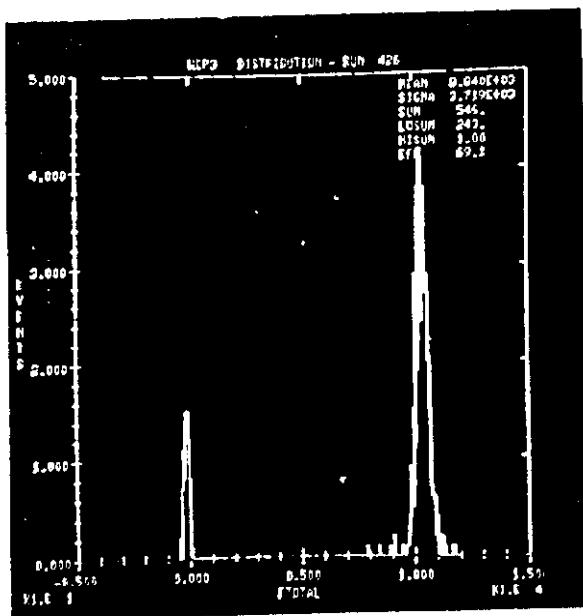
Fig. 20



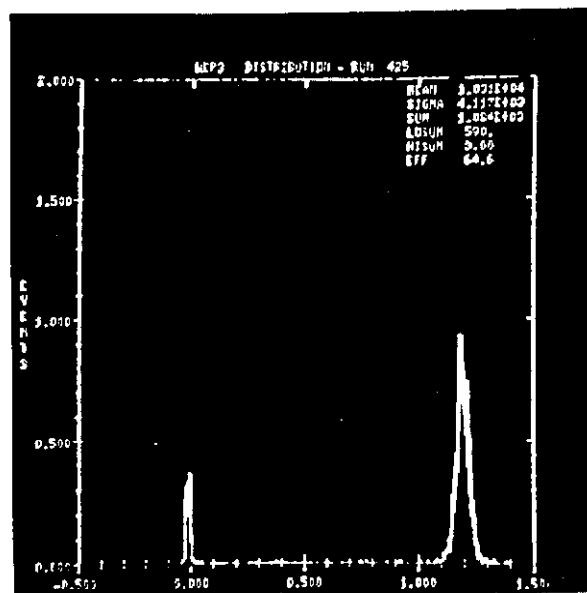
a 50 GeV  
1.8 kV



b 100 GeV  
1.8 kV



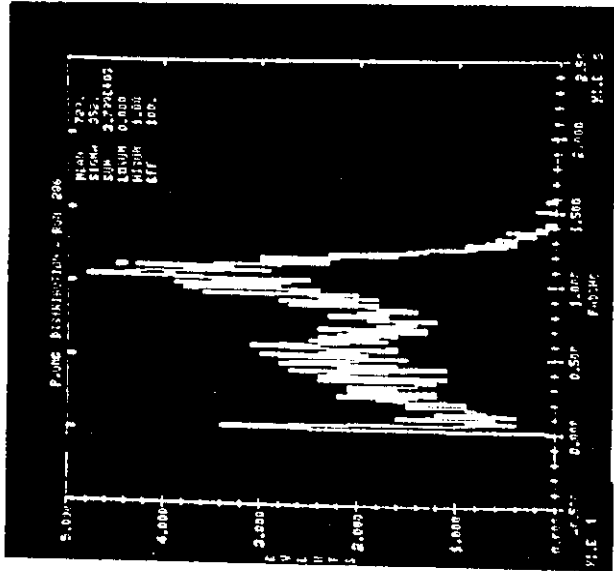
c 150 GeV  
1.8 kV



d 175 GeV  
1.8 kV

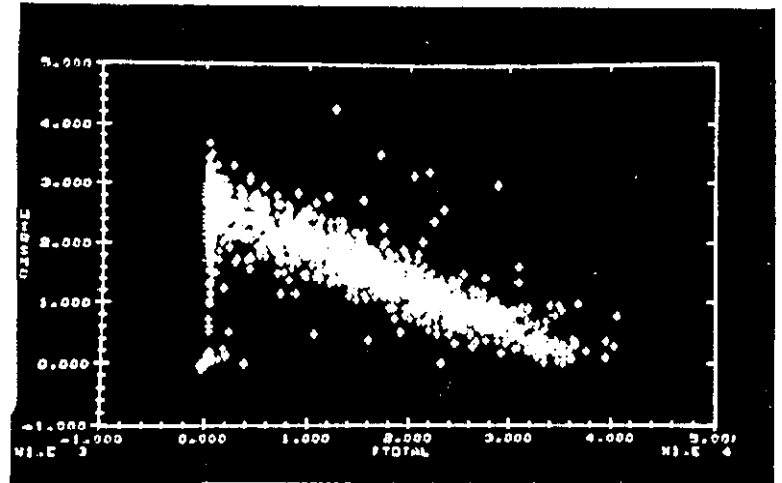
Fig. 21

150 GeV Pions



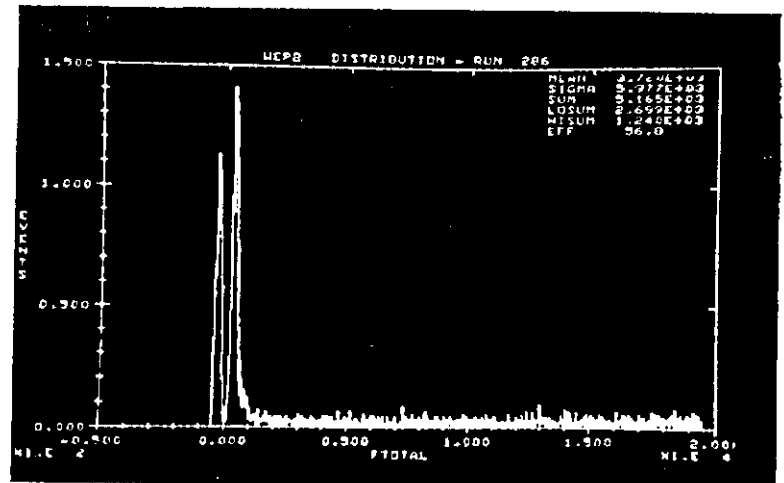
b

HADRON CALORIMETER



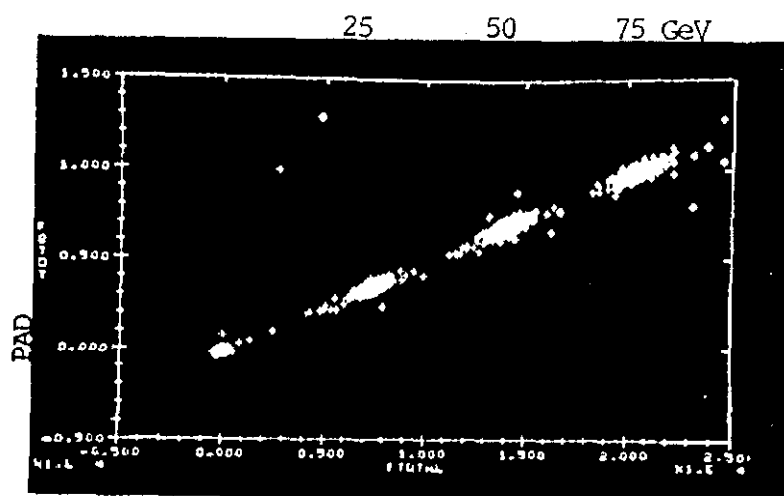
c

E.M. CALORIMETER



a

Fig. 22



1.95 kV

Ar-ETHANE 50%-50%  
ETHYLALCOHOL 1.4%

50  $\mu$ m WIRE

Fig. 23

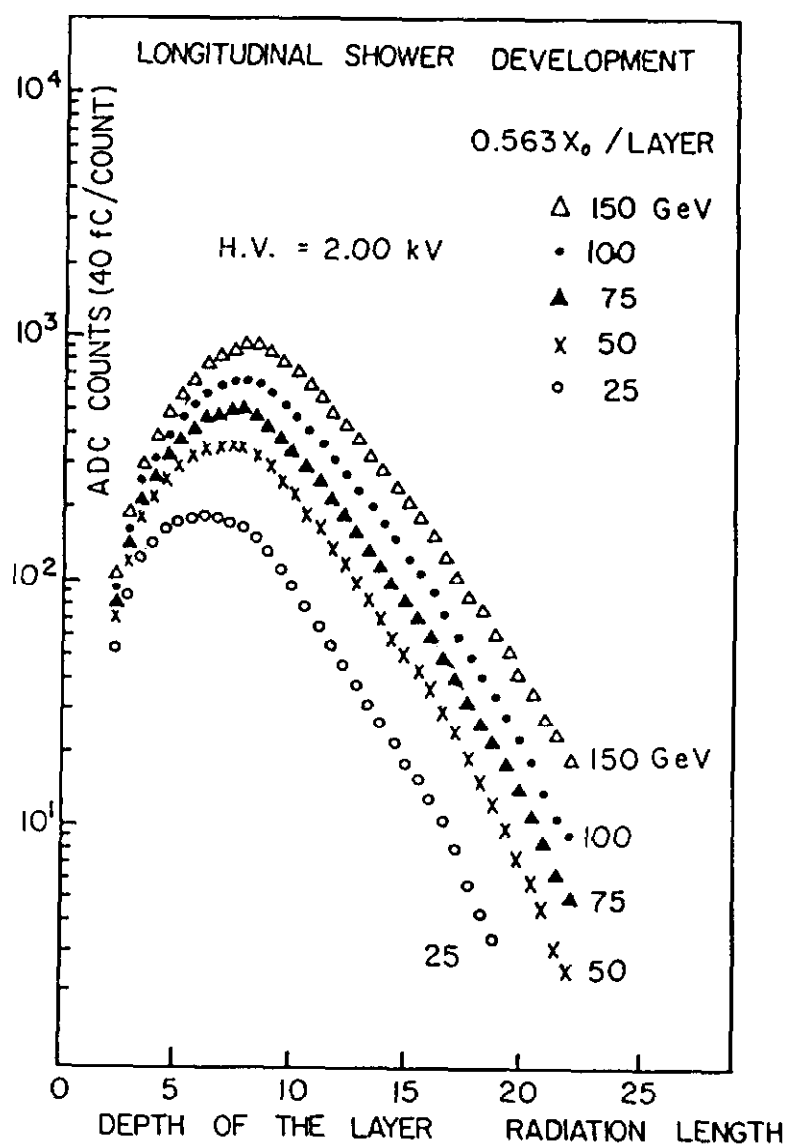
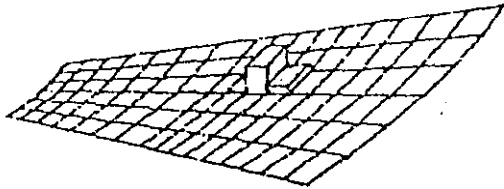
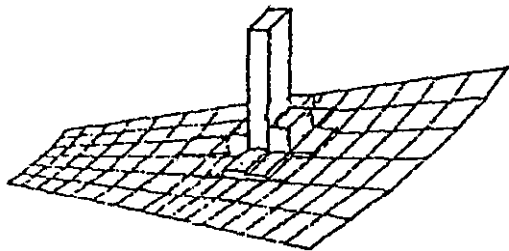


Fig. 24

1ST SEGMENT



2ND SEGMENT



3RD SEGMENT

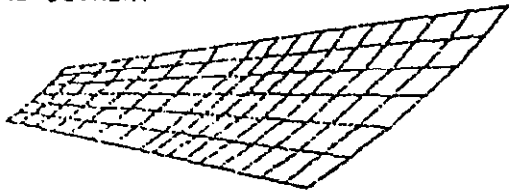
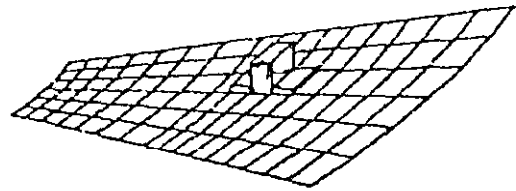
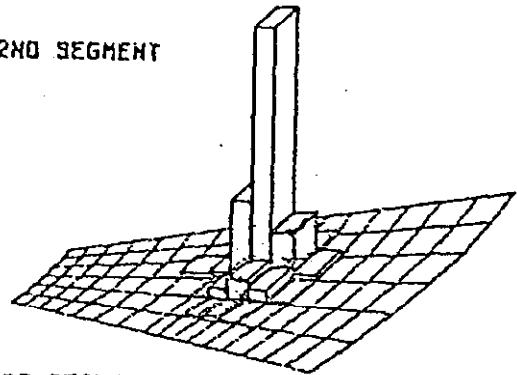


Fig. 25 a. 50 GeV Electron

1ST SEGMENT



2ND SEGMENT



3RD SEGMENT

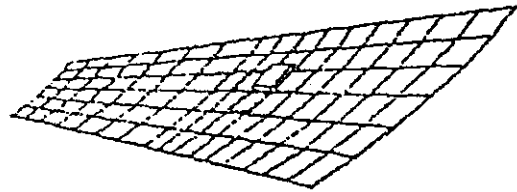
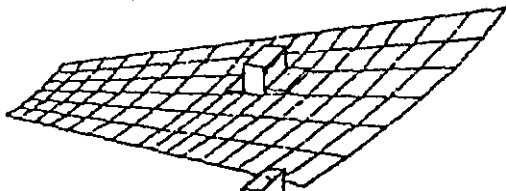
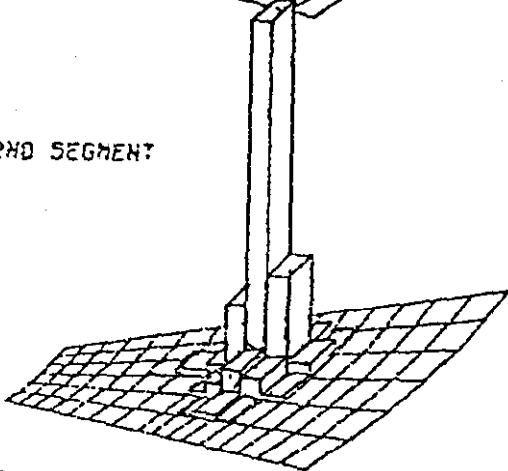


Fig. 25 b. 100 GeV Electron

1ST SEGMENT



2ND SEGMENT



3RD SEGMENT

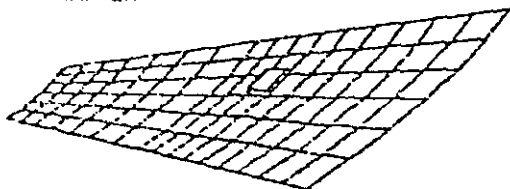
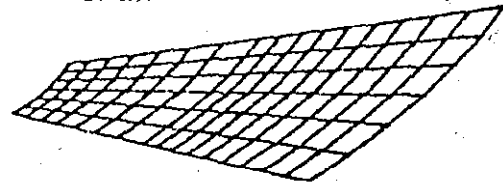
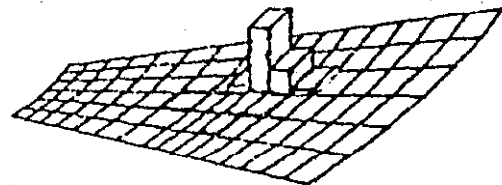


Fig. 25 c. 150 GeV Electron

1ST SEGMENT



2ND SEGMENT



3RD SEGMENT

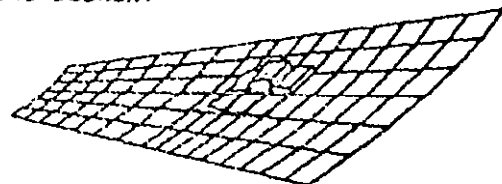


Fig. 26. 100 GeV Pion

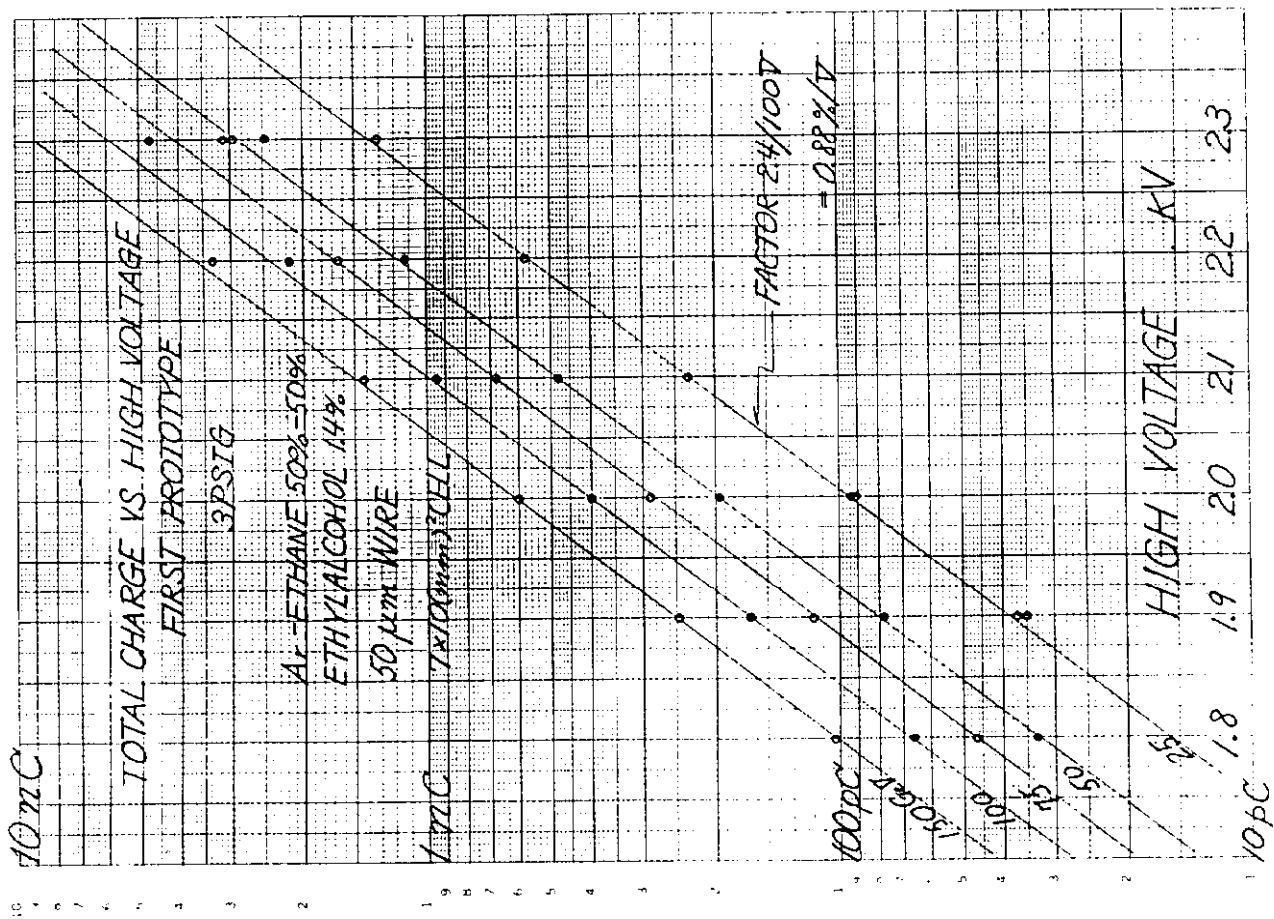


Fig. 28

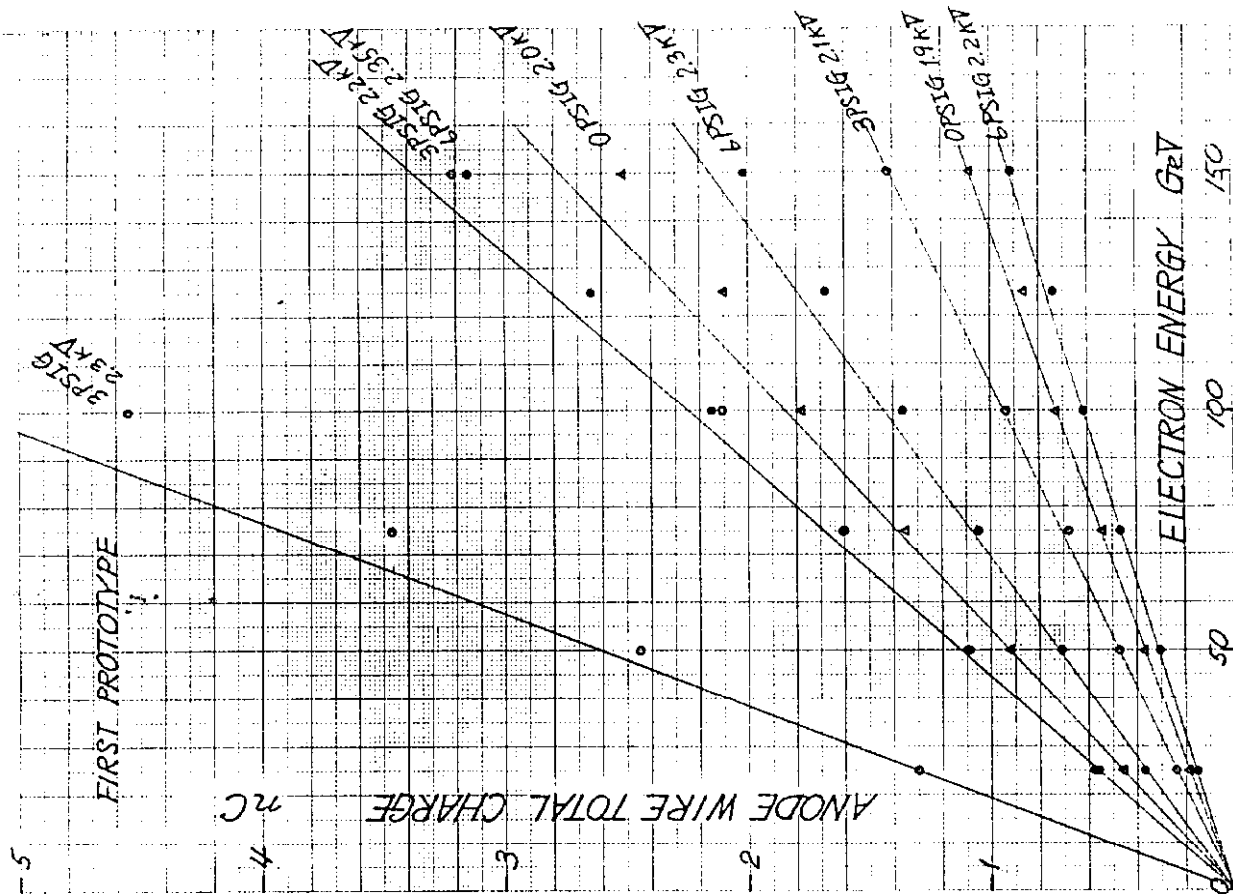


Fig. 27

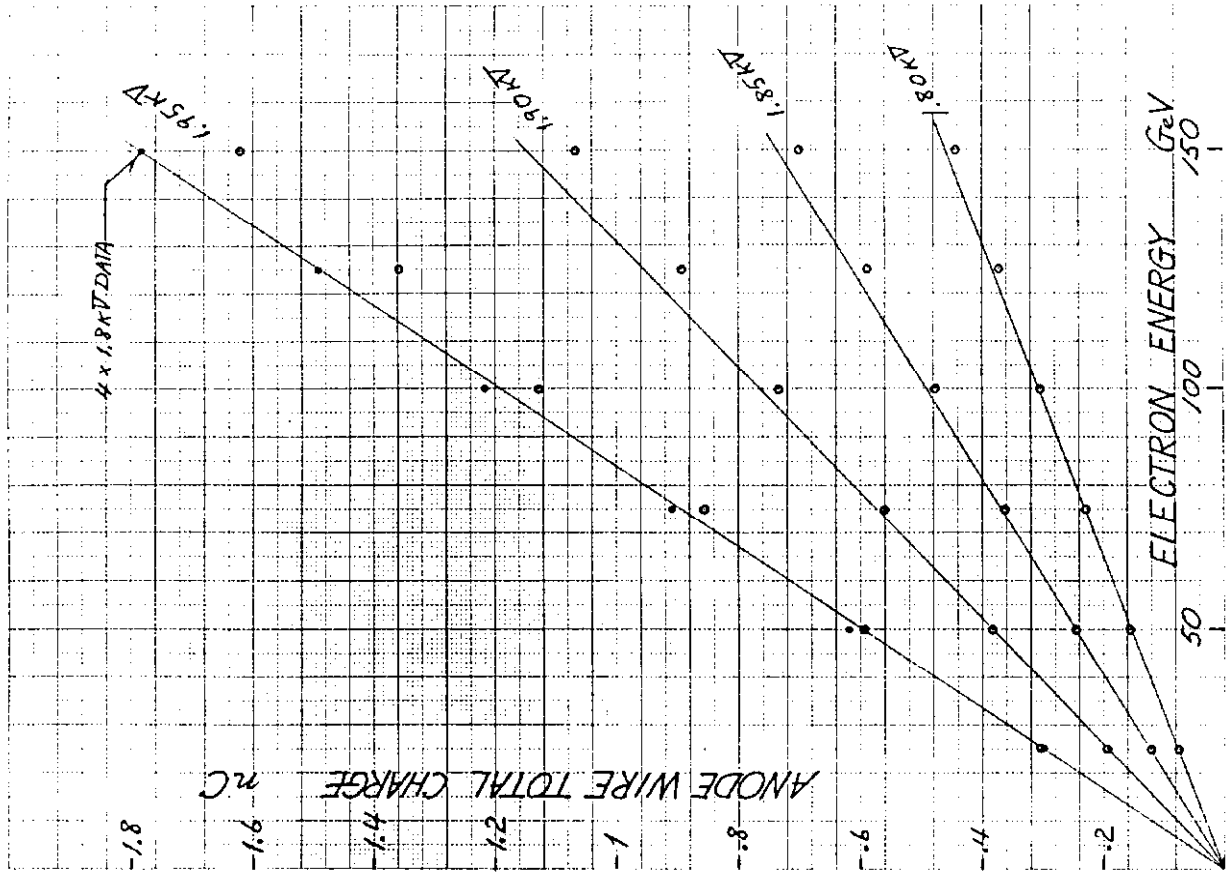


Fig. 29

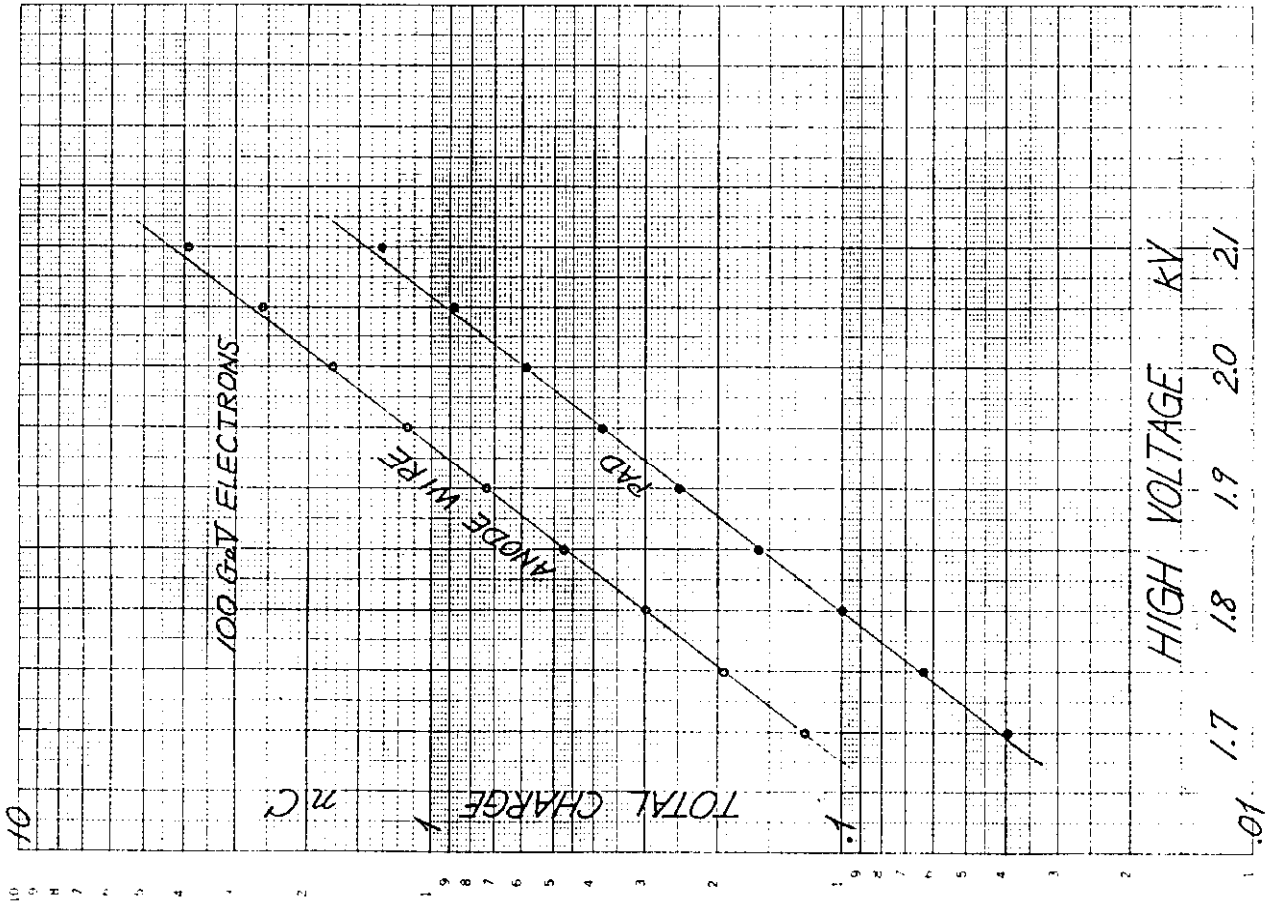


Fig. 30

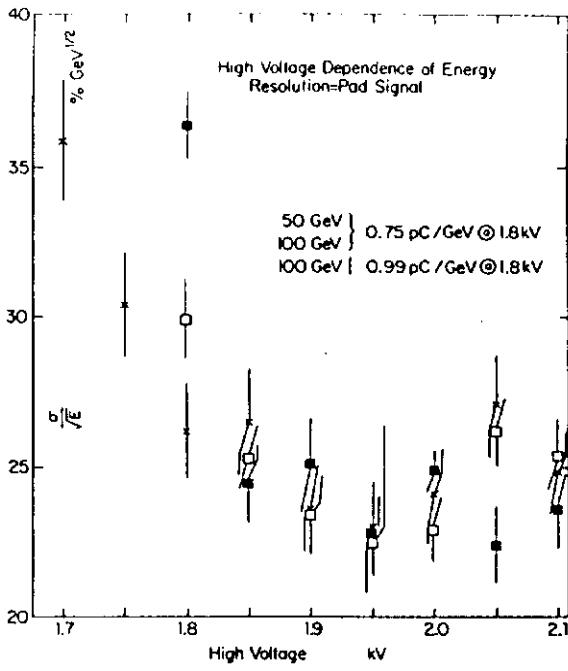


Fig. 31

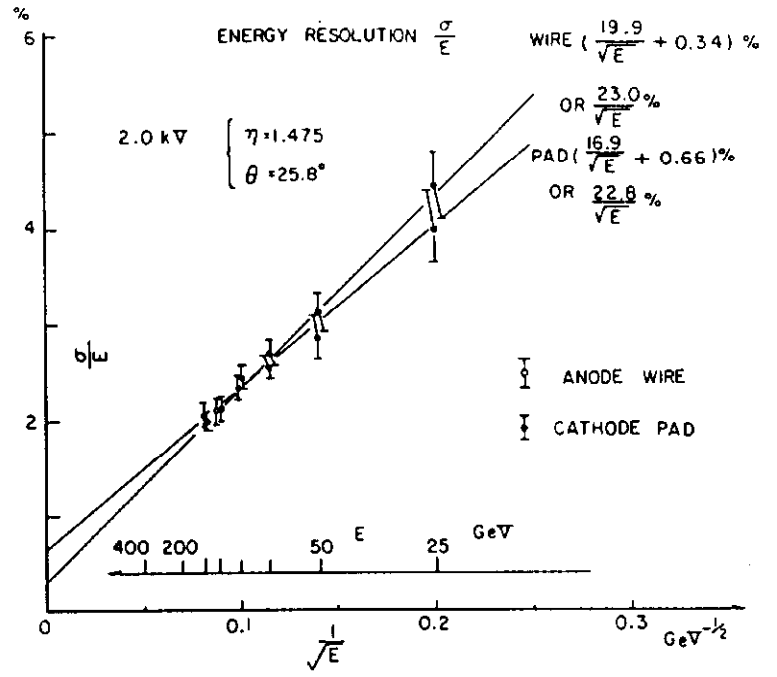


Fig. 32

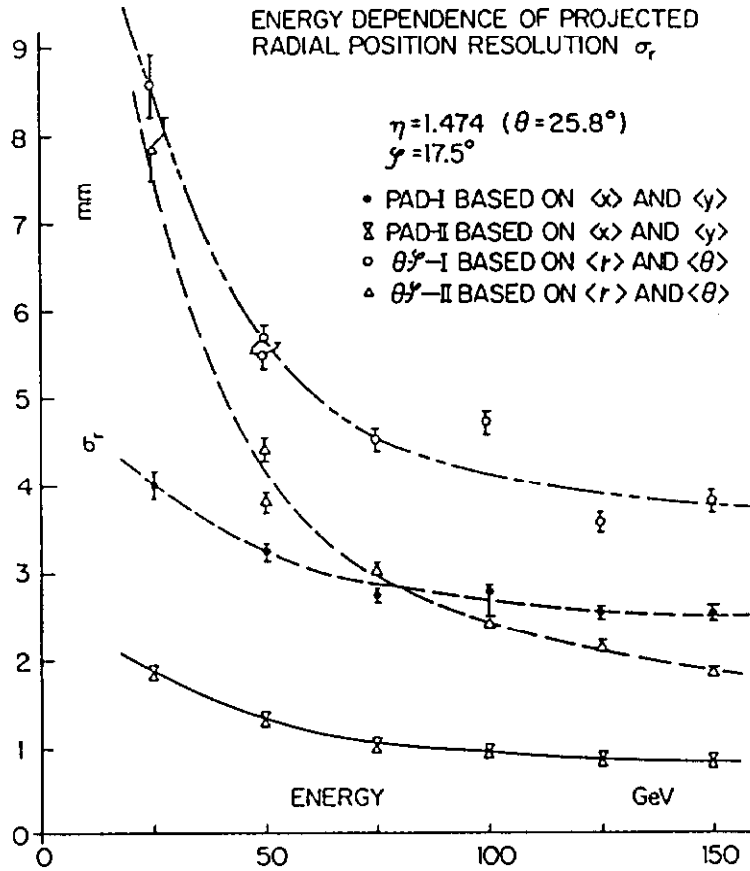


Fig. 33

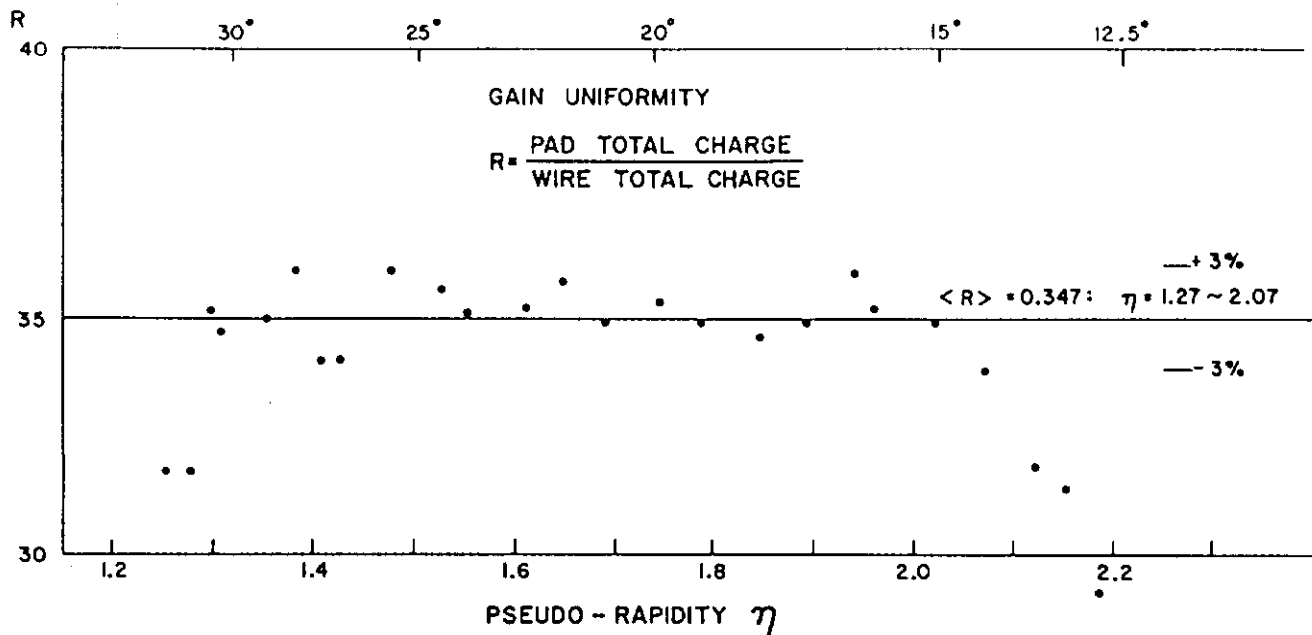


Fig. 34

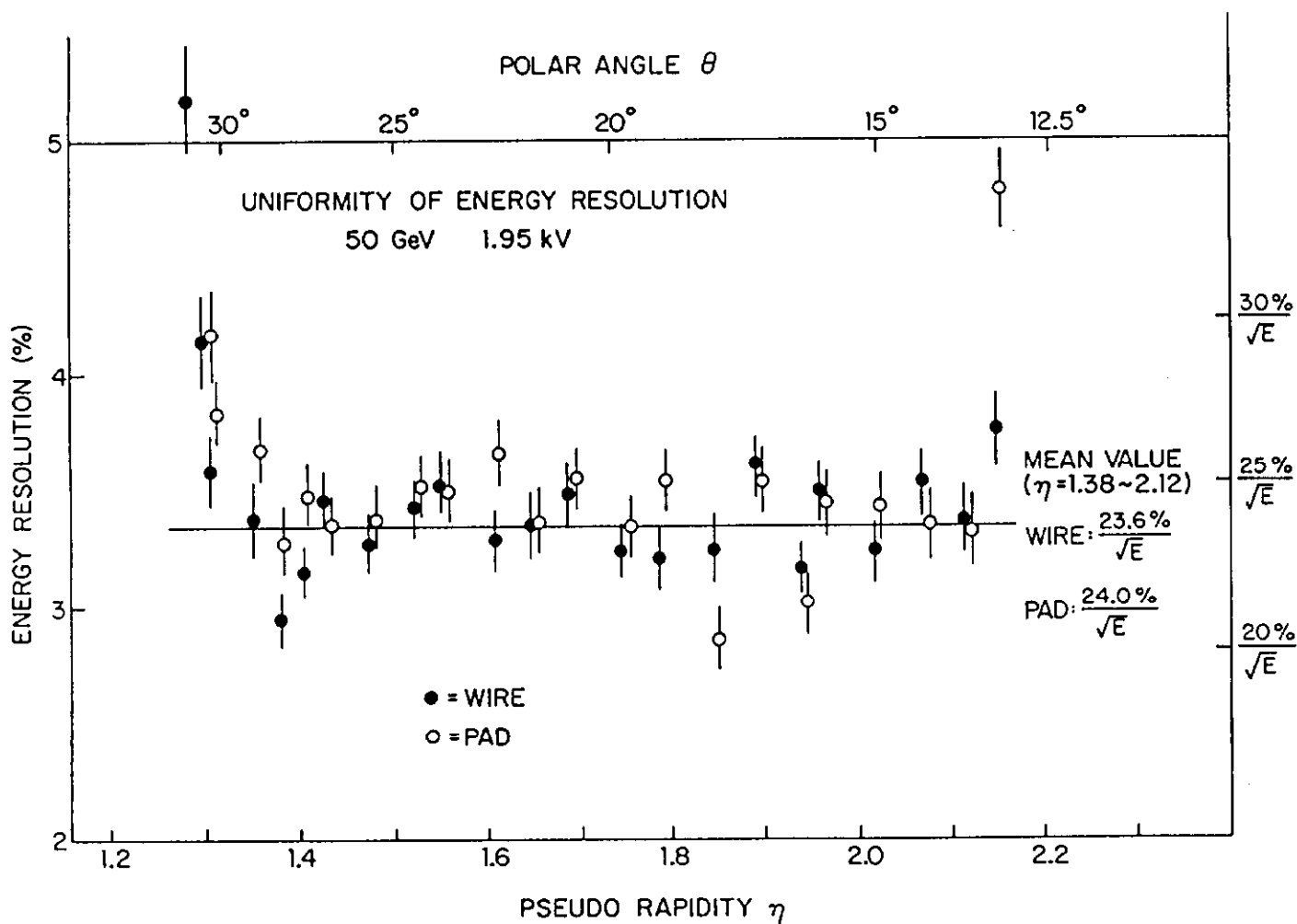


Fig. 35

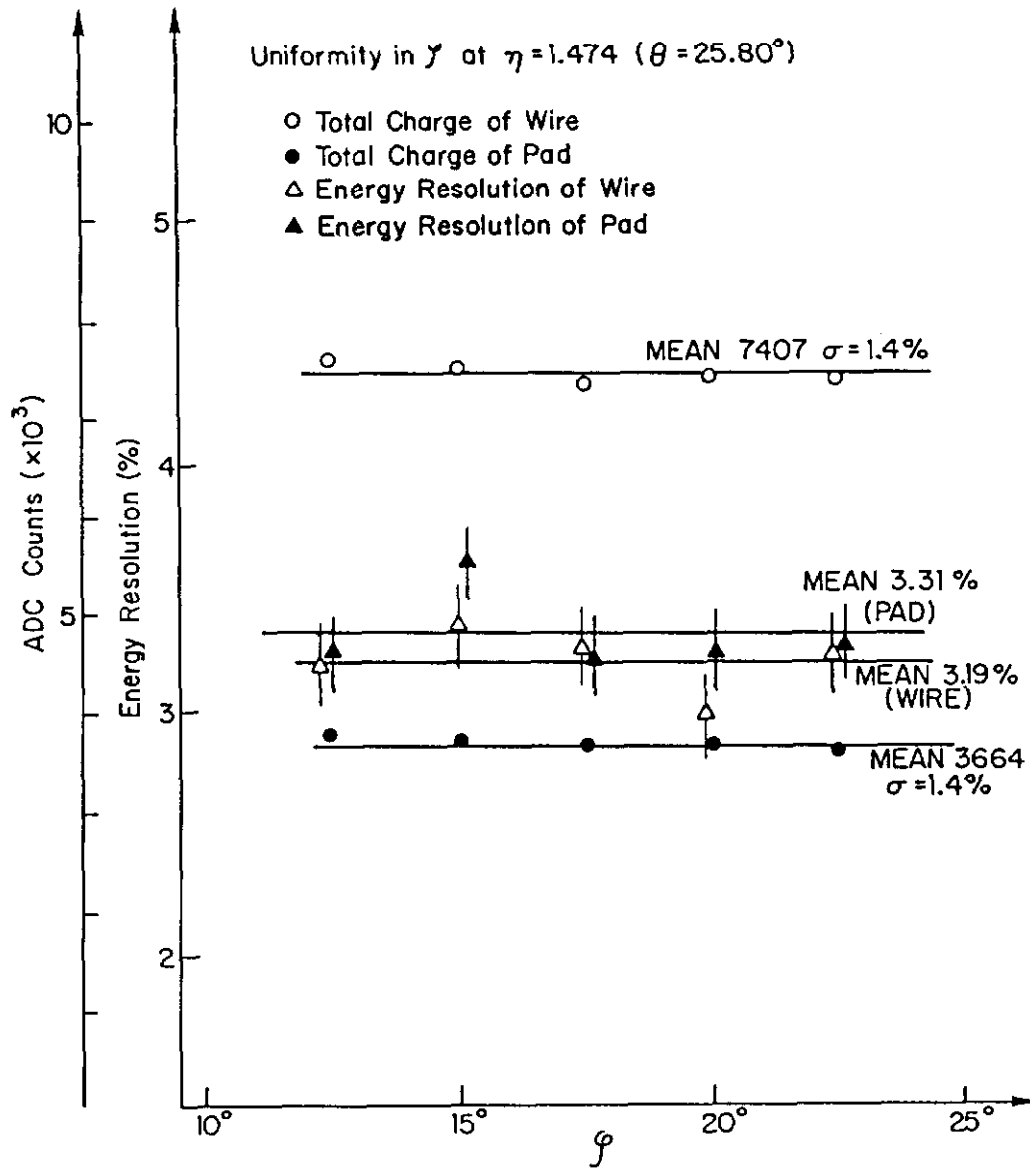


Fig. 36

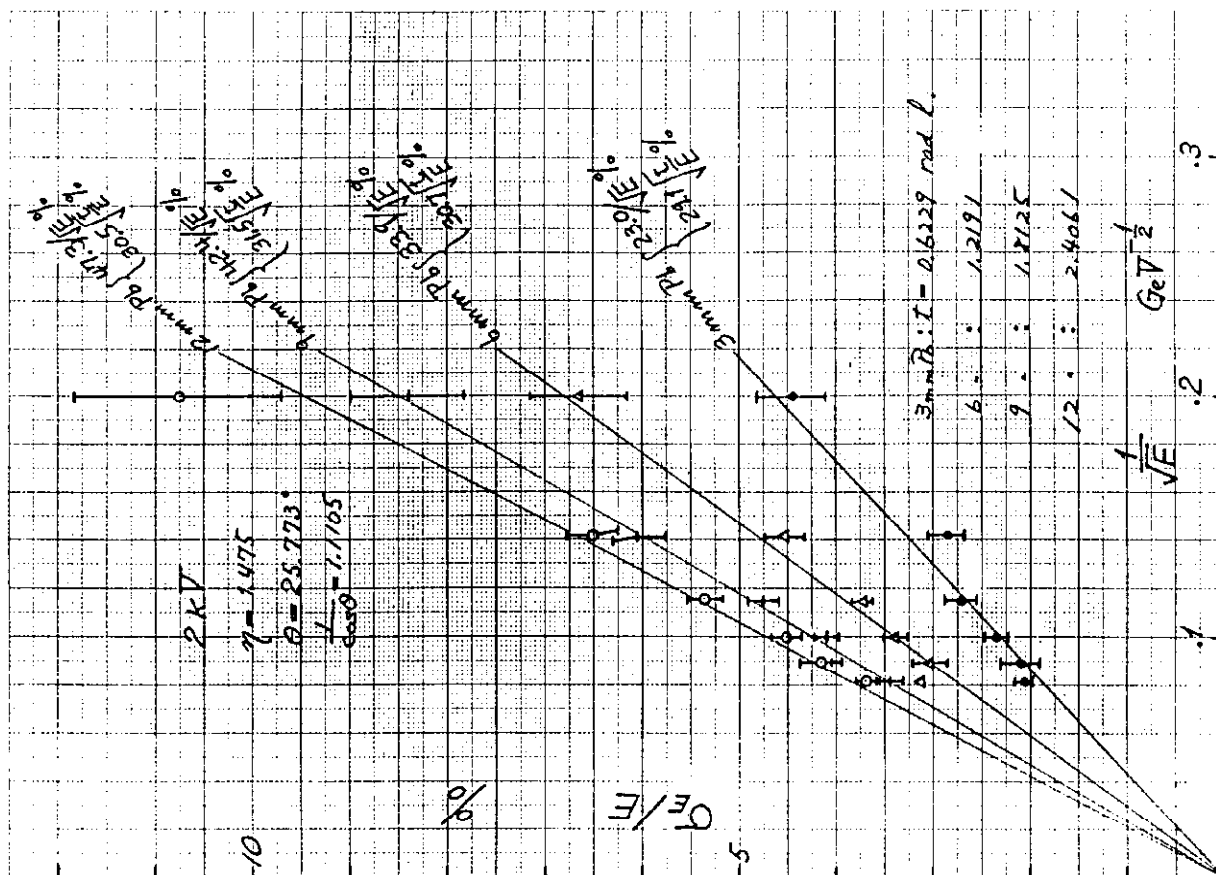


Fig. 37

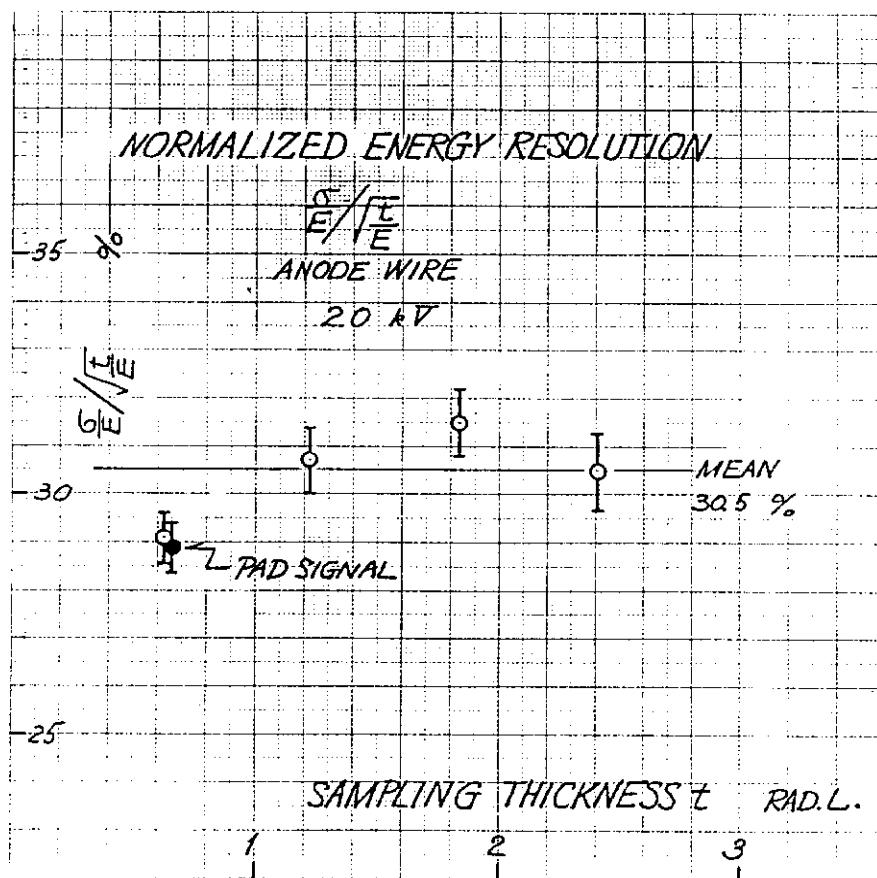


Fig. 38

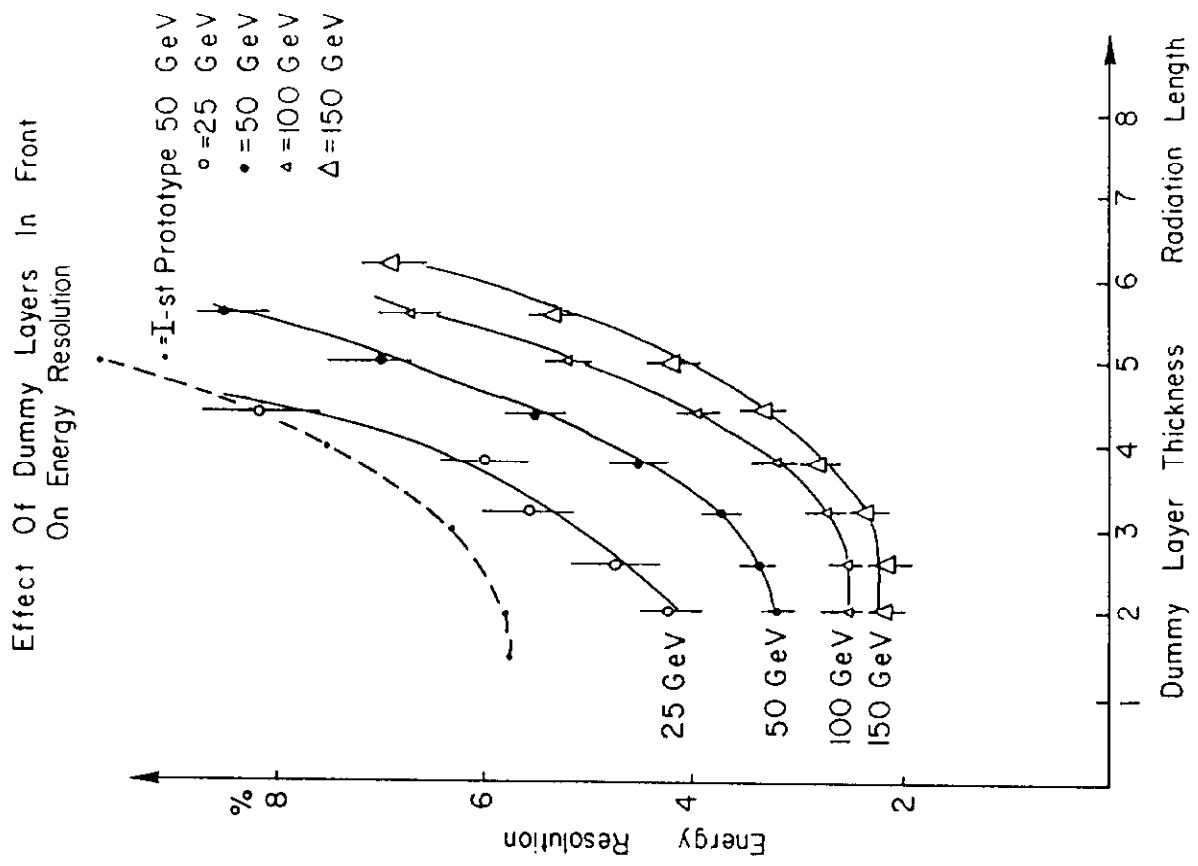


Fig. 39

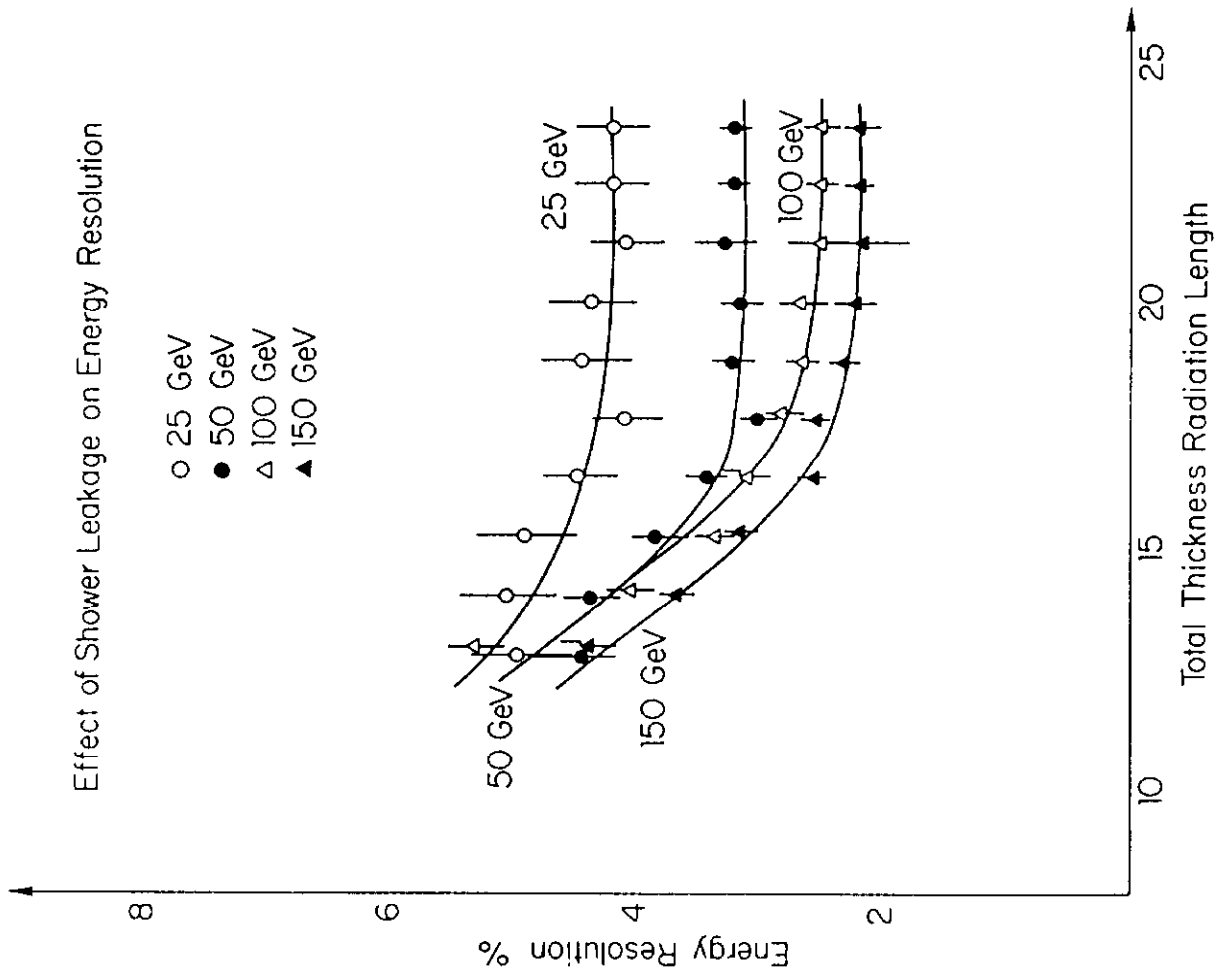


Fig. 40

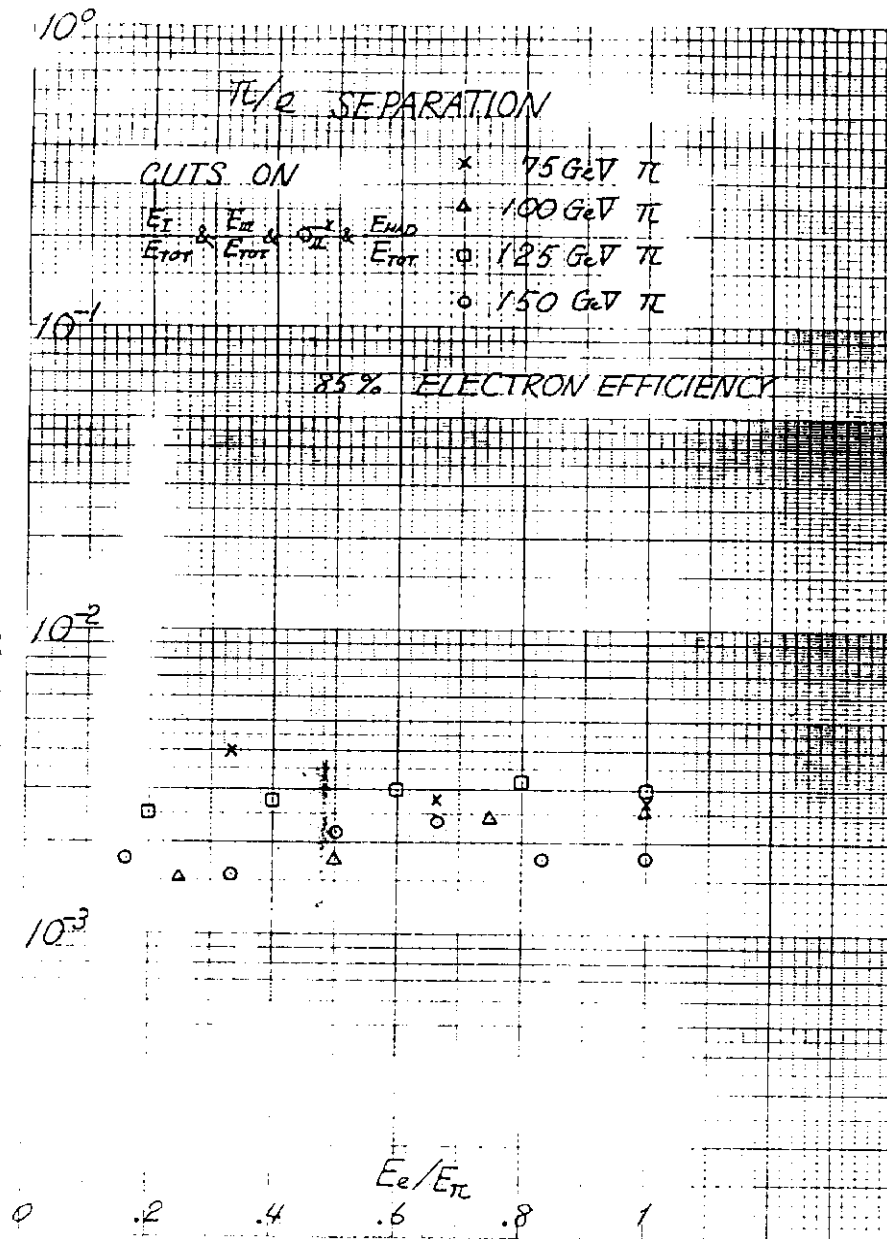


Fig. 42

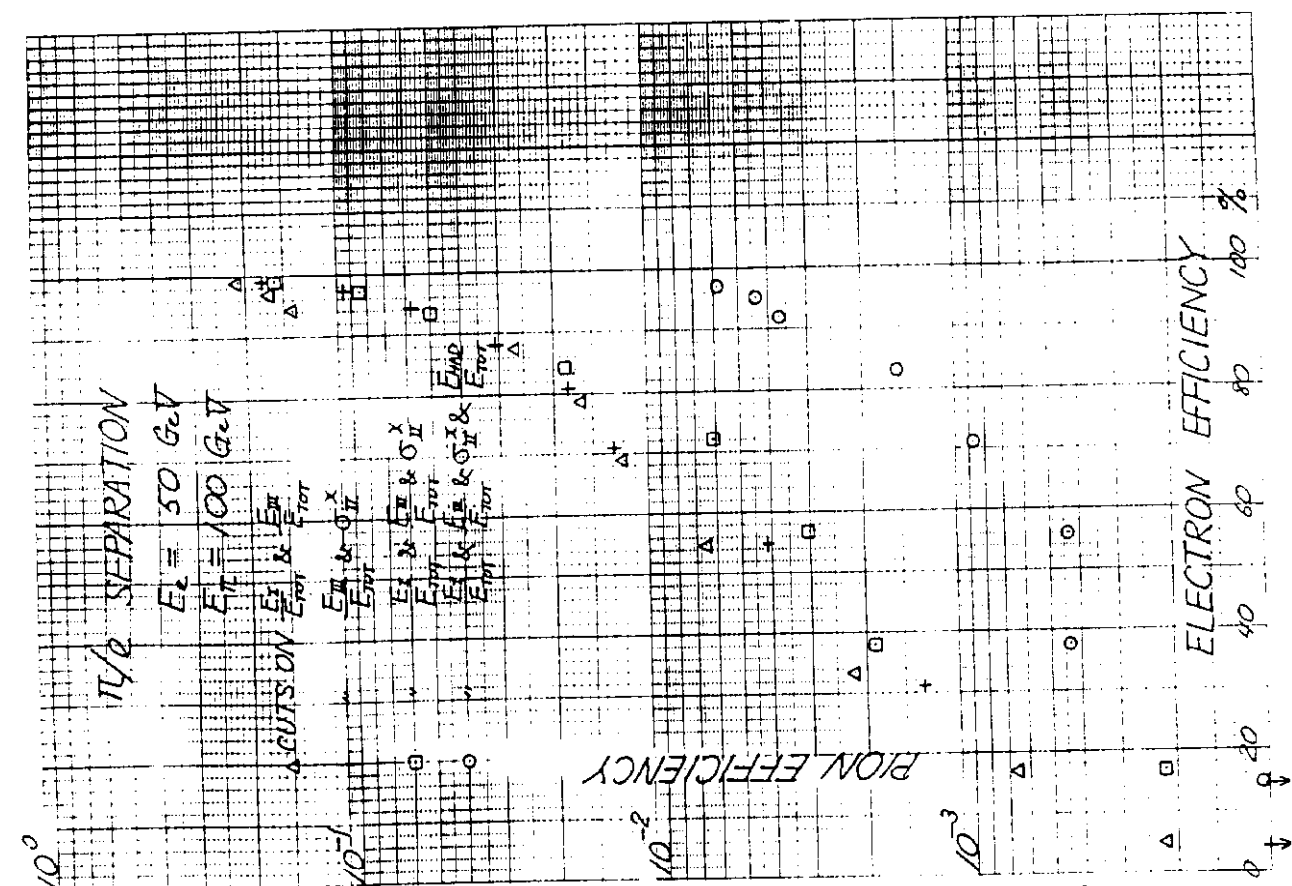


Fig. 41 b

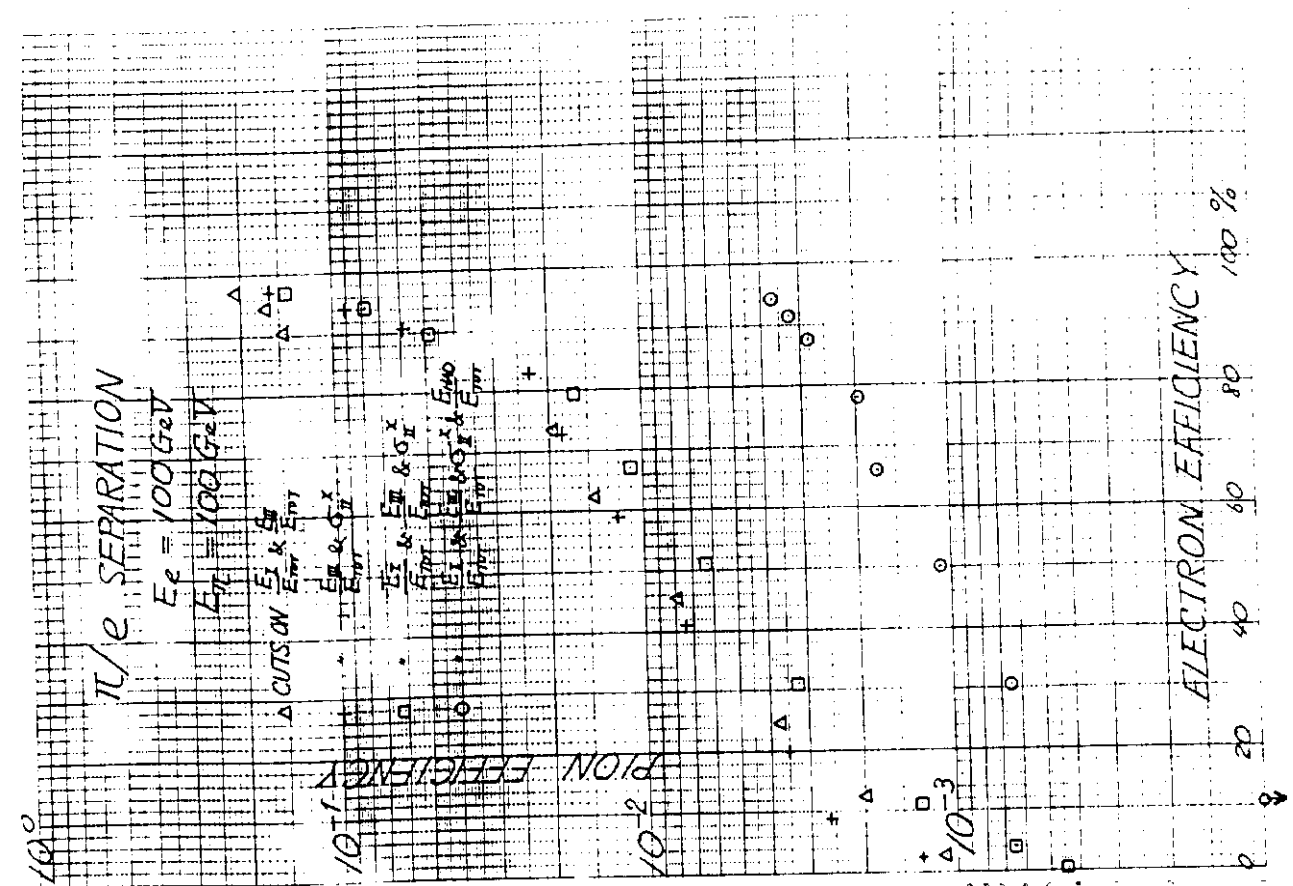


Fig. 41 a